

# The Value-Added Catalog of ASAS-SN Eclipsing Binaries II: Properties of Extra-Physics Systems

D. M. Rowan,<sup>1,2\*</sup> T. Jayasinghe<sup>1,2,3,4</sup>, K. Z. Stanek<sup>1,2</sup>, C. S. Kochanek<sup>1,2</sup>, Todd A. Thompson<sup>1,2,5</sup>,  
B. J. Shappee<sup>6</sup>, T. W. -S. Holoien<sup>7</sup>, J. L. Prieto<sup>8,9</sup>, and W. Giles<sup>10</sup>

<sup>1</sup>*Department of Astronomy, The Ohio State University, 140 West 18th Avenue, Columbus, OH, 43210, USA*

<sup>2</sup>*Center for Cosmology and Astroparticle Physics, The Ohio State University, 191 W. Woodruff Avenue, Columbus, OH, 43210, USA*

<sup>3</sup>*Department of Astronomy, University of California Berkeley, Berkeley CA 94720, USA*

<sup>4</sup>*NASA Hubble Fellow*

<sup>5</sup>*Department of Physics, The Ohio State University, Columbus, Ohio, 43210, USA*

<sup>6</sup>*Institute for Astronomy, University of Hawaii, 2680 Woodlawn Drive, Honolulu, HI 96822, USA*

<sup>7</sup>*Carnegie Observatories, 813 Santa Barbara Street, Pasadena, CA 91101, USA*

<sup>8</sup>*Núcleo de Astronomía de la Facultad de Ingeniería y Ciencias, Universidad Diego Portales, Av. Ejército 441, Santiago, Chile*

<sup>9</sup>*Millennium Institute of Astrophysics, Santiago, Chile*

<sup>10</sup>*ASC Technology Services, 433 Mendenhall Laboratory 125 South Oval Mall Columbus OH, 43210, USA*

Accepted XXX. Received YYY; in original form ZZZ

## ABSTRACT

Detached eclipsing binaries are the primary tool used to measure precise masses and radii of stars. In our previous paper estimating the parameters of more than 30,000 detached eclipsing binaries, we identified 766 eclipsing binaries with additional features in their All-Sky Automated Survey for Supernovae (ASAS-SN) and Transiting Exoplanet Survey Satellite (TESS) light curves. Here, we characterize these “extra-physics” systems, identifying eclipsing binaries with spotted stars, pulsating components, and candidate triple/quadruple systems. We use the Gaia, ATLAS, ZTF, and ASAS-SN variable star catalogs to consider possible blends. We use MIST isochrones and evolutionary tracks to identify systems with main sequence, subgiant, and giant primaries and highlight systems in sparsely populated regions of the color-magnitude diagram. We find that the orbital period distribution of spotted binaries is divided by evolutionary state and find 68 with X-ray detections. For the candidate triple/quadruples and pulsating systems, we calculate the extra orbital/pulsational period and identify systems with resonances. Finally, we highlight a number of exotic systems, including eclipsing CVs, subdwarfs, and binaries with disks.

**Key words:** binaries:eclipsing – surveys

## 1 INTRODUCTION

One of the primary applications of eclipsing binaries is to determine the physical parameters of stars. By modeling their light curves and radial velocities, precise masses and radii can be determined and used to validate and improve models of stellar structure (e.g., Andersen 1991; Torres et al. 2010). Photometric and spectroscopic surveys have discovered tens of thousands of binary stars (Graczyk et al. 2011; Prša et al. 2011; Petrosky et al. 2021; Pojmanski 2002; Jayasinghe et al. 2019a, 2021; Christy et al. 2022; Pourbaix et al. 2004). Interesting subsets of systems can then be identified from such large catalogs, such as extremely eccentric binaries (e.g., Zasche et al. 2021), systems with changing eclipse depths (e.g., Davenport et al. 2021), and triple and quadruple eclipsing systems (e.g., Rappaport et al. 2022; Kostov et al. 2022; Zasche et al. 2022).

Eclipsing binaries are traditionally classified into four morphological classes. Detached eclipsing binaries or Algol-type binaries have essentially spherical stars with no obvious effects of ellipsoidal vari-

ability in the light curve. Semidetached systems ( $\beta$ -Lyrae) have one or both stars nearly filling their Roche lobes, and contact binaries (W Uma) fill their Roche lobes. Finally, ellipsoidal variables are binaries where the modulations from tidal distortion dominate the overall light curve shape, often without observed eclipses (e.g., Rowan et al. 2021). The majority of eclipsing binary catalogs use these four classifications (e.g., Jayasinghe et al. 2019a), although some catalogs instead use a continuous variable to describe the ‘detachedness’ of the binary (Matijević et al. 2012; Prša et al. 2022).

Subclasses of eclipsing binaries have also been introduced for eclipsing binaries with additional light curve features. For example, the RS Canum Venaticorum-type binary systems (RS CVn) have increased stellar activity and spots producing sinusoidal features in the light curve that change over time. The identification and modeling of eclipsing RS CVn systems can be used to improve our understanding of stellar activity cycles and the evolutionary history of the binary (Roettenbacher et al. 2016).

Pulsational variability of one or both of the components in an eclipsing binary can be used to study stellar structure in greater detail (Kahraman Aliçavuş et al. 2017). Properties of the interior structure

\* E-mail: rowan.90@osu.edu

of the star can be determined by modeling the pulsation characteristics, and the physical mass and radius can be determined by modeling the light curve and radial velocity curve. These systems can also be used to understand how pulsations are affected by the gravitational force of the binary companion (Soydugan et al. 2006a). Eclipsing binaries containing various types of pulsators have been identified, including  $\delta$  Scuti (Soydugan et al. 2006b; Shi et al. 2022),  $\gamma$  Dor (Damiani et al. 2010), and Cepheid (Gieren et al. 2015) variables.

Eclipsing binary catalogs have also aided in the search for systems with a third body or doubly-eclipsing binaries. The detection and analysis of these systems can be used to improve our understanding of the frequency of higher-order systems, their formation mechanisms, and the dynamical processes that shape their evolution. Tertiary companions can be identified in binary systems by monitoring the eclipse timing variations over timescales much longer than the orbital period (Borkovits et al. 2015). Depending on the orbital inclination of the third body, they can also be discovered by detecting additional eclipses (Marsh et al. 2014; Rappaport et al. 2022). Similarly, quadruple systems made up of two pairs of eclipsing binaries can be found by searching for additional periods in the light curves of known eclipsing binaries (Kostov et al. 2022; Zasche et al. 2022). Catalogs of doubly eclipsing binaries suggest an excess of systems with 3:2 period ratios (Zasche et al. 2019) which can be used to inform models of resonant capture (Tremaine 2020).

Machine learning techniques are almost always used to classify variable stars, including eclipsing binaries. However, the detection of unusual subclasses of systems, like pulsating eclipsing binaries or doubly eclipsing binaries, is still often done through visual inspection. In Rowan et al. (2022, hereafter R22), we visually inspected more than 40,000 eclipsing binary light curves from the All-Sky Automated Survey for Supernovae (ASAS-SN, Shappee et al. 2014; Kochanek et al. 2017) and Transiting Exoplanet Survey Satellite (TESS, Ricker et al. 2015; Kunimoto et al. 2021; Huang et al. 2020a,b) to verify our eclipsing binary models. In the process of we also identified 766 systems that could not be described by simple models of eclipsing binaries due to the presence of spots, pulsations, or additional eclipses.

Here we present the ASAS-SN  $V$ , ASAS-SN  $g$ , and TESS  $T$  band light curves and discuss the properties of these 766 eclipsing binaries with extra physics. In Section §2, we describe the ASAS-SN and TESS light curves and the visual inspection process used to identify and classify these light curves. In Section §3, we show the distribution of light curve parameters, including the Gaia DR3 CMD position. Sections §3.1–3.6, we describe the properties of the different variability classes and calculate the periods of pulsations, triples, and quadruple systems when applicable. Finally, we characterize unique systems that do not fall into the groups discussed in Section §2 in Section §3.7.

## 2 LIGHT CURVES AND TARGET IDENTIFICATION

In R22, we modeled the ASAS-SN  $V$ - and  $g$ -band light curves of more than 30,000 detached eclipsing binaries from Jayasinghe et al. (2021). The  $V$ -band light curves span from 2012 to mid 2018 and the  $g$ -band observations have been ongoing since late 2017. The optimal magnitude range for ASAS-SN targets is  $11 < V < 17$  mag and  $12 < g < 18$  mag (Jayasinghe et al. 2019a).

We used PHOEBE (Prša & Zwitter 2005; Prša et al. 2016; Conroy et al. 2020), a tool for modeling eclipsing binaries of all morphological classes, to fit the ASAS-SN light curves, and then we visually inspected all the model fits to identify systems that required addi-

tional optimization. As a part of this process, we downloaded the TESS light curves from the the SPOC (Caldwell et al. 2020) and QLP (Huang et al. 2020a,b) pipelines. We use the “raw” light curves rather than the detrended light curves since the detrending procedure can often remove real stellar variability. We folded the TESS light curves at the period calculated from the ASAS-SN light curves and identified 766 targets that showed additional features in the ASAS-SN or TESS light curves. At the time of writing (October 2022), TESS light curves are available for 734 of our targets.

We broadly group these systems by the nature of the “extra physics” seen in the light curve:

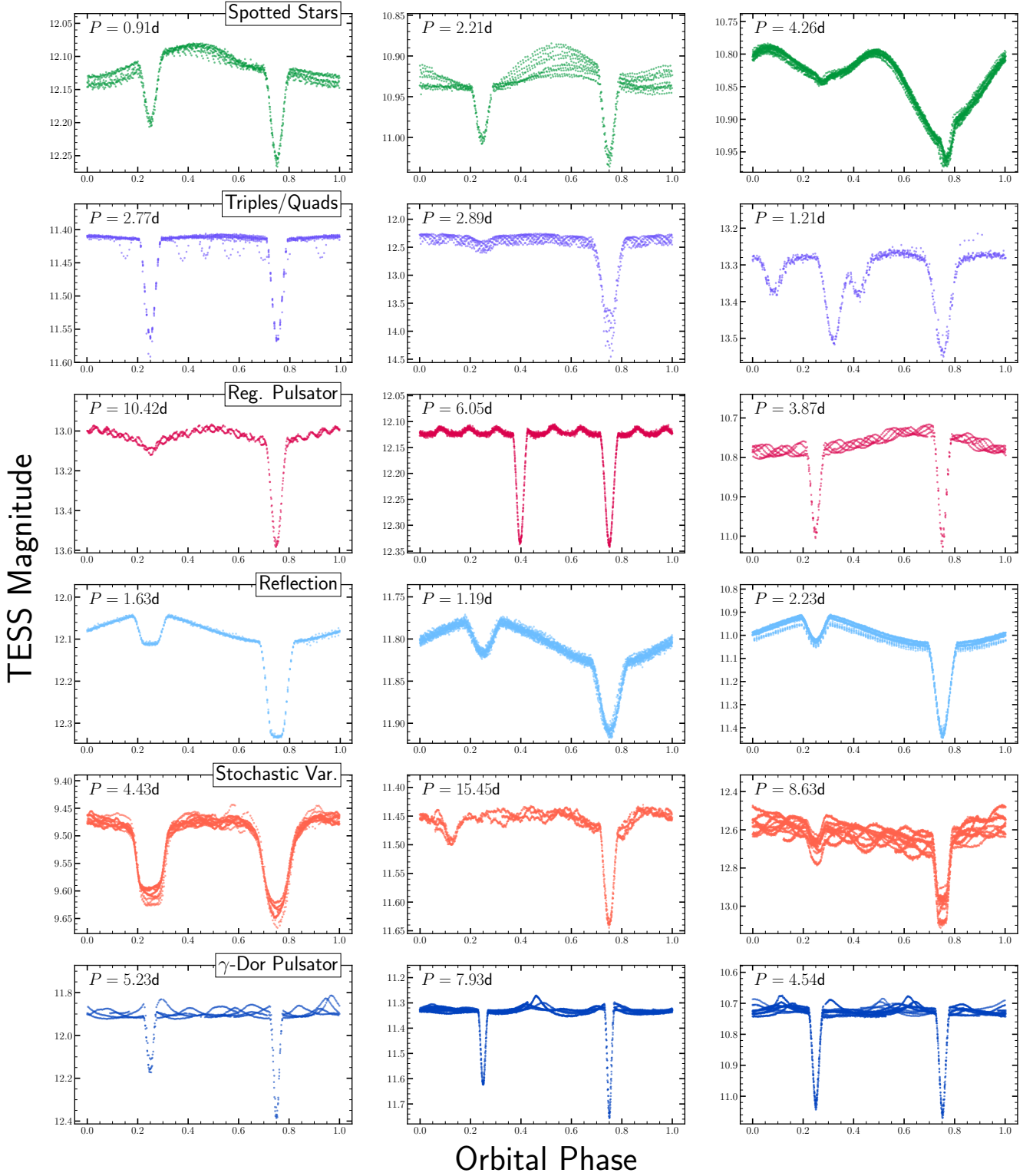
- Spotted stars: 426 targets
- Triple and doubly eclipsing binaries: 225 targets
- Reflection effects: 29 targets
- Regular pulsators: 36 targets
- Stochastic variability: 24 targets
- $\gamma$ -Dor pulsators: 17 targets
- Other: 9 targets

Figure 1 shows the TESS light curves for example systems from each group. The largest group are the spotted systems (426 targets) where one or more spots distort the overall shape of the light curve. In some cases the amplitude and phasing of the spots changes over the course of the TESS sector or between sectors. The next largest group are the systems with extra eclipses (225 targets) from a tertiary or an additional eclipsing binary. In the phased light curve, these systems are identified as having additional eclipses at a different orbital period. We also identify 36 systems showing regular, periodic pulsations, as well as 17 binaries with more  $\gamma$ -Dor-like variability and 24 systems with stochastic variability. Finally, we identify 29 systems where the large temperature differences between the components results in an overall brightening of the light curve near the secondary eclipse due to irradiation. There are also 9 targets that do not fit into any of these categories. These are discussed in Section 3.7. The full set of light curves are available online at <https://asas-sn.osu.edu/binaries>. Table 1 gives the parameters of each system and their classification into the groups listed above.

## 3 CATALOG DESCRIPTION

Figure 2 shows the distribution of the systems on the sky. Since the TESS pixels are  $21''$  and typical aperture radii range from 1.75 to 8 pixels (Huang et al. 2020a), it is possible that some of these systems, especially those with extra eclipses, are actually blended sources. To quantify how many of these targets may be blends, we cross-match with the ATLAS all-sky stellar reference catalog (ATLAS REF CAT2, Tonry et al. 2018). The ATLAS  $r1$  proximity statistic gives the radius where the cumulative flux of nearby stars equals the flux of the target up to a search radius of  $36''$ . Targets  $r1 < 36''$  are more likely to be blends. Out of the 766 extra-physics targets, 138 have  $r1 < 36''$ . In Figure 2 the targets with  $r1 < 36''$  are marked with black borders and we see these are concentrated in the Galactic plane.

If a target is actually a blend, we may expect to find multiple matches to variability catalogs for a single source. We cross-match our catalog with the Gaia DR3 (Gaia Collaboration et al. 2022), ZTF (Chen et al. 2020), ATLAS (Heinze et al. 2018), and ASAS-SN (Jayasinghe et al. 2021; Christy et al. 2022) variability catalogs with a search radius of  $21''$ . All of these surveys have higher resolution than TESS, so blended targets are more likely to be identified as distinct variable sources. For the Gaia crossmatch, we take all targets within



**Figure 1.** TESS light curves for examples of the different variability types. The orbital period is labeled in the upper left of each panel. The light curves are folded so that the primary eclipse occurs at phase 0.75.

**Table 1.** Parameters of the extra-physics sample. The  $r_1$  statistic comes from the ATLAS REFCAT-2 catalog and is set at 99.9 if the cumulative flux from nearby stars does not equal the flux of the target within  $36''$ . The Gaia absolute magnitude ( $M_G$ ) and color ( $G_{BP} - G_{RP}$ ) are corrected for extinction using `mw dust`. The evolutionary state is calculated based on the procedure described in R22.  $P_2$  gives the period of the pulsations or additional eclipses. The reference column gives the citation for triple/quadruple systems included in existing catalogs. The full table is available online at <https://asas-sn.osu.edu/binaries> and in the electronic version of the paper.

Gaia DR3 Source	Period (d)	Group	$r_1$ (")	$M_G$ (mag)	$G_{BP} - G_{RP}$ (mag)	State	$P_2$ (d)	Reference	$L_X$ (erg/s)	X-ray Sep. (")	X-ray Obs.
4634512158994726144	6.0387	Spotted Stars	99.9	5.74	1.27		6.0311				
2880801592412343552	16.0311	Spotted Stars	99.9	3.05	1.10	SG	16.0906				
4991376490493277952	0.9505	Spotted Stars	99.9	4.92	0.89	MS	0.9470		$1.3 \times 10^{31}$	3.9	SWIFT
430569204423511552	0.8485	Triples/Quads	99.9	3.28	0.63	MS	3.5177				
431081611195489536	2.3547	Triples/Quads	99.9	-2.35	0.12	SG					
524420699465597184	4.0792	Triples/Quads	99.9	-1.40	0.21	SG	4.9867	Z22,K22			
401523955495860608	16.7389	Reg. Pulsator	99.9	1.71	0.54	MS	0.9513				
457177145291803776	3.4892	Reg. Pulsator	99.9	-0.78	0.05		0.5307				
457720785072612480	4.6068	Reg. Pulsator	99.9	-0.10	0.23	MS	1.0575				
513586146241283072	1.6320	Reflection	99.9	-1.01	0.37					0.3	CHANDRA
465551472526065152	1.3211	Reflection	99.9	-1.78	-0.04	MS			$1.5 \times 10^{31}$	1.1	XMM-NEWTON
3449142279545037056	1.6192	Reflection	99.9	-1.30	0.04	MS					
511009646904766336	11.7224	Stochastic Var.	99.9	-3.96	0.08						
461470115422532352	2.1279	Stochastic Var.	99.9	-1.98	-0.04	SG					
491478678258597632	3.1399	Stochastic Var.	99.9	2.43	0.79	SG					
351850661555541504	5.2264	$\gamma$ -Dor Pulsator	99.9	2.69	0.58	MS					
23092256739885312	5.6819	$\gamma$ -Dor Pulsator	99.9	1.98	0.48	MS					
435896716209335040	8.2931	$\gamma$ -Dor Pulsator	99.9	2.15	0.51	MS					
4687138015328580736	15.0812	Other	99.9	-2.36	-0.12						
4655260836825948160	27.1112	Other	21.9	-2.87	-0.67						
6055907396399148032	2.5331	Other	99.9	1.61	0.63	MS					

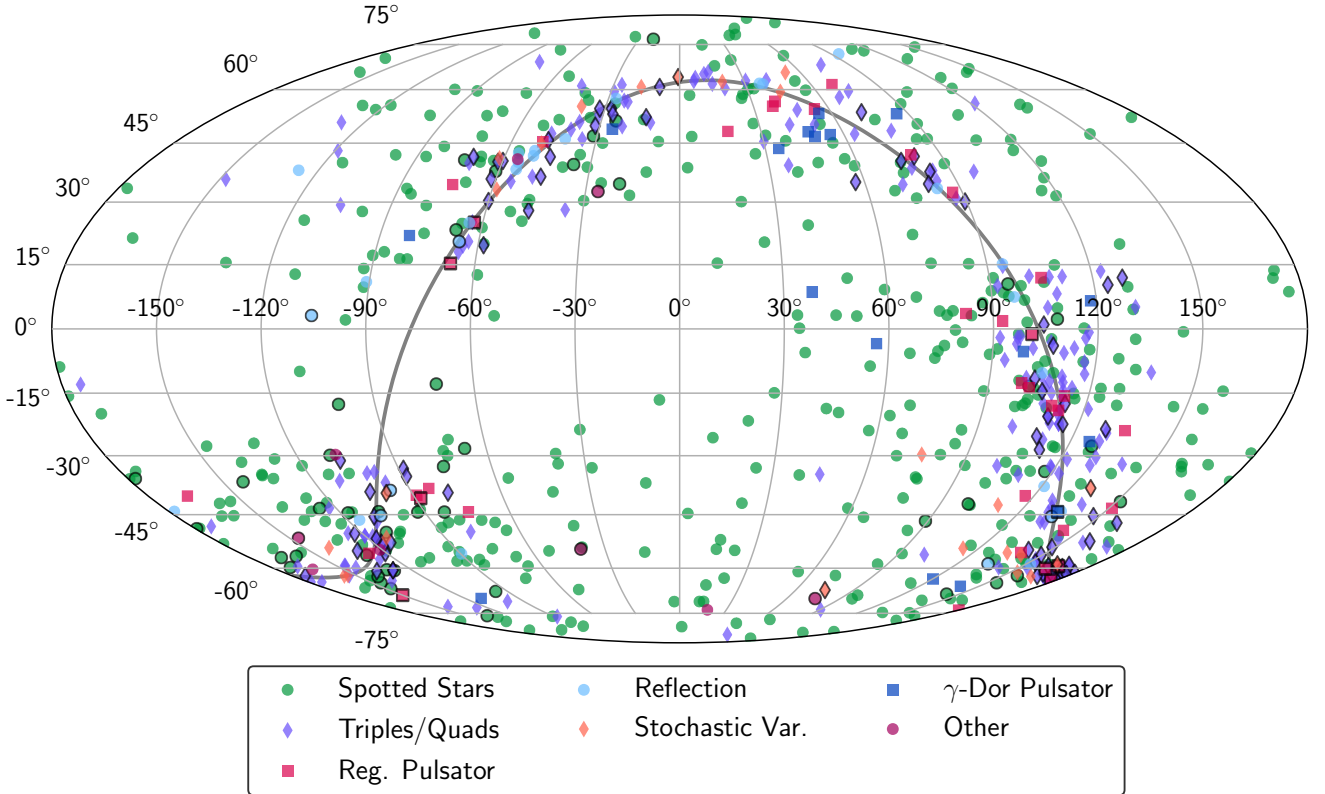


**Figure 2.** Sky distribution of the extra-physics targets in equatorial coordinates. The Galactic plane is the gray line. Targets are colored by their variability type. Targets with  $r_1 < 36''$  are shown with black borders. We find an excess of targets near the Galactic plane with  $r_1 < 36''$ , especially for systems showing extra eclipses, suggesting some could be blends due to the low resolution of TESS.

**Table 2.** Cross matches of the extra-physics targets to the Gaia, ZTF, and ATLAS variability catalogs with a radius of  $21''$ . The Gaia Source and magnitude from Table 1 are given in the first two columns. The  $P_2$  column reports the Gaia, ZTF, or ATLAS period if it is within 5% the rotation period, spotted period, or second orbital period in the TESS light curve. The full table is available online at <https://asas-sn.osu.edu/binaries> and in the electronic version of the paper.

DR3 Source	$G$ (mag)	Nearby DR3 Source	$G$ (mag)	Gaia Sep. (" $''$ )	ZTF ID	$g$ (mag)	ZTF Sep. (" $''$ )	ATLAS ID	$o$ (mag)	ATLAS Sep. (" $''$ )	$P_2$ (d)
183120431790693120	12.9							J083.5330+35.2988	16.2	14.0	
198407697866912128	11.5							J073.9465+37.3475	16.1	20.2	
200791134137604352	13.8							J074.9785+40.4087	13.6	0.0	3.787
219832339066395264	11.6	219832339066395392	12.1	2.5							
239043654764555520	13.1							J046.7897+39.9546	15.6	11.3	
273109278071250944	13.8				J044752.88+533026.5	15.3	7.8				
337798490636307968	12.6				J022611.88+391415.8	14.7	8.2				13.685
355800111620808576	12.5				J020003.55+452605.2	13.0	6.1	J030.0148+45.4347	12.7	6.1	0.589
434846854403757184	13.9							J049.0648+46.7908	15.4	8.1	
434846854403757184	13.9							J049.0645+46.7950	15.8	13.5	
447114998986540672	12.0							J046.9632+54.0670	14.3	8.8	
447114998986540672	12.0							J046.9594+54.0661	11.9	0.0	2.407
505860530871568512	13.4	505860526571955712	19.6	8.8	J014430.68+572555.5	20.4	8.8				
510360419650993920	13.0				J012033.99+602257.2	18.0	19.8				
524381426285320064	13.5				J005638.57+652706.8	17.8	9.4				

$21''$  that have the `phot_variable_flag` set to “variable”. The Gaia variability catalog may be less reliable for evaluating the blending of triple/quadruple systems, since detached eclipsing binaries are less likely to be identified in the sparse, sigma-clipped Gaia light curves. Out of the 766 targets in our catalog, only 518 binaries (67.6%) are identified as variable in Gaia DR3. For the ZTF cross-match, we consider targets in the main variability catalog and the suspected variable catalog (Tables 2 and 3 of Chen et al. 2020). Only 372 and 80 binaries are identified as variables in the ATLAS and ZTF catalogs, respectively, but we note that these catalogs are not all-sky.

We also compare the Gaia, ATLAS, and ZTF periods, when available, to the orbital period,  $P$ , and the second orbital period,  $P_2$  (calculated as described below in Sections §3.1, §3.2 and §3.4). We check if the periods given in the variability catalogs are within 5% of  $P$  or  $P_2$ , and also check for aliases at half and double these periods. With the ZTF catalog, we compare with the  $g$ - and  $r$ -band periods, and for ATLAS we compare with the periods from the long-period Fourier fit, short-period Fourier fit, and Lomb-Scargle periodogram. For the Gaia variables, we consider the periods corresponding to the fundamental and first overtone mode of variables in the RR Lyrae and Cepheid catalogs, the periods in the short- and long-timescale variability catalogs, the main sequence oscillator periods, rotation periods, and eclipsing binary periods.

To remove the variable star entry corresponding to the original ASAS-SN eclipsing binary in the Gaia cross-match, we simply check that the Gaia Source is different from the that of the original ASAS-SN source. For the ATLAS and ZTF cross-match, we assume that the variable star corresponds to the original ASAS-SN eclipsing binary if the ATLAS/ZTF period is consistent with  $P$ , or if it is separated by  $< 5''$ . We also flag any variable with separation  $< 21''$  where the period is within 5% of  $P_2$  (or its aliases) as the highest confidence blended targets.

Table 2 reports the available matches. In total, 108 of our binaries are found to have nearby variable stars. The largest number of matches are found in Gaia DR3 (59 matches), followed by ATLAS (45 matches), and ZTF (19 matches). We find no matches in the ASAS-SN  $V$ - and  $g$ -band catalogs. The triple/quadruple systems have the most number of possible blended variables (54 binaries)

followed by spotted stars (34 binaries). The remaining groups have  $< 10$  systems with nearby variable stars. We find that 20 of these systems have periods potentially consistent with the period of the extra eclipses or the pulsation period. These systems have the most evidence for being blends in the TESS light curves, but we note that seven of these nearby variables are separated by  $< 5''$ , which may indicate that the system is either a blend of two unresolved binaries in the ZTF or ATLAS light curves, or is truly multi-periodic, with the second period being reported in the ATLAS/ZTF/Gaia catalogs, rather than the “main” orbital period.

Additional checks for blended targets could use the expected amplitude of the variability. Even if the amplitude of the extra eclipses or pulsations is small in the TESS light curves, nearby, faint ( $G \sim 17$  mag) stars can still cause contamination if the amplitude of the variability in the blended variable is large. We do not compare the expected amplitudes here because of the challenges in comparing amplitudes from catalogs that use different filters.

Figure 3 shows the distributions of the apparent  $G$ -band magnitudes and orbital periods. The majority of our targets are at periods shorter than a TESS sector, but we identify some extra-physics targets at longer periods using the ASAS-SN light curves. Many of these targets are bright enough for radial velocity followup, which could be used to confirm the triple/quadruple system candidates.

We cross-match our catalog with Gaia Data Release 3 (GDR3, Gaia Collaboration et al. 2022) and the catalog of distances from Bailer-Jones et al. (2021). We combine the color and distance information with extinction estimates from the `mw dust` (Bovy et al. 2016) 3-dimensional ‘Combined19’ dust map (Drimmel et al. 2003; Marshall et al. 2006; Green et al. 2019). We use the MESA Isochrones & Stellar Tracks (MIST, Choi et al. 2016; Dotter 2016) to divide the color-magnitude diagram (CMD) into systems with main sequence and giant/subgiant primaries. Following R22, we only report the evolutionary state for systems with `parallax_over_error`  $> 10$  and  $A_V < 2.0$  mag. Figure 4 shows the extra-physics systems on a CMD colored by their variability type.

Since rotational variability in particular can produce high-energy emission, we cross-matched our catalog with the HEASARC Mas-

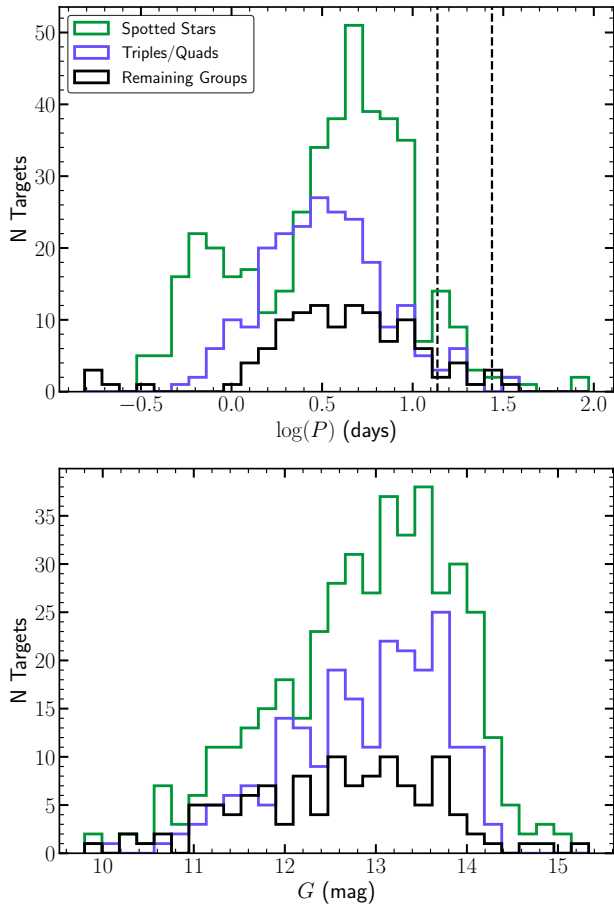


**Figure 3.** Top: distribution of orbital periods. Even though these targets were originally selected from the multi-year ASAS-SN data, we find that the majority of targets have periods shorter than the TESS orbit/sector length, shown by the vertical dashed lines. Bottom: the distribution of Gaia  $G$  magnitudes.

ter X-ray catalog<sup>1</sup> and the Swift-XRT Point Source Catalog (Evans et al. 2020), both with a search radius of  $10''$ . In the HEASARC Master X-ray catalog, we find X-ray sources in ROSAT (Voges et al. 1999), XMM-Newton (Jansen et al. 2001), and Chandra (Evans et al. 2010) catalogs, which all have different localization errors, so X-ray sources at larger separations should be confirmed. In total, we find X-ray matches for 74 targets, 68 of which are spotted binaries. The remaining systems are in the reflection, triples/quadruples, regular pulsator, and other groups. Table 1 reports the X-ray luminosity,  $L_X$ , computed using the Bailer-Jones et al. (2021) distance measurements, and the angular separation between the X-ray and optical position. For targets with multiple X-ray matches we use the flux corresponding to the longest exposure to compute  $L_X$ . We next discuss each group in order of their size.

### 3.1 Spotted Stars

The distribution of the orbital periods of the spotted eclipsing binaries is bimodal (Figure 3). The short period sample is almost exclusively

<sup>1</sup> <https://heasarc.gsfc.nasa.gov/W3Browse/all/xray.html>

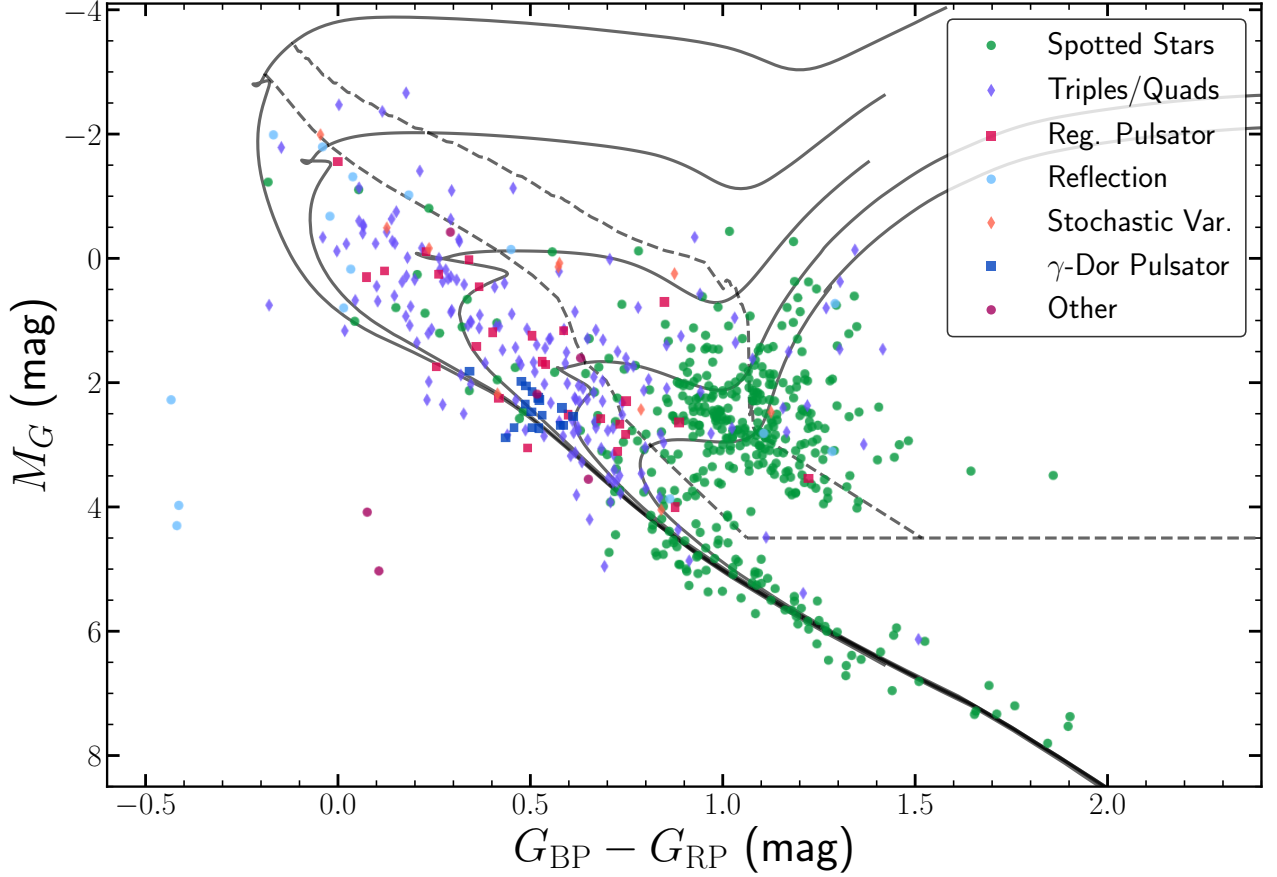
made up of systems with MS primaries, and the longer periods are SG and RG systems. The median orbital period of the MS spotted binaries is 0.91 days and the median period of the SG and RG systems is 5.4 days. This division by evolutionary state is relatively pure – only 26 (20.5%) MS have periods  $\log(P) > 0.3$  days and 11 (3.9%) of SG and RG systems have periods shorter than  $\log(P) < 0.3$  days. In total, 68 of spotted binaries have X-ray detections within  $10''$ . Compared to the full sample of spotted binaries, the systems with X-ray emission tend to have shorter periods. The MS spotted binaries with X-ray emission have a median orbital period of 0.65 days compared to 0.91 days and the median period of the SG/G spotted systems decreases from 5.4 days to 4.7 days.

Figure 5 shows the distribution of extinction-corrected absolute  $K$ -band magnitude,  $M_K$ , and  $\log P$  for the spotted binaries. Christy et al. (2022) identified unique ‘clumps’ of rotational variables in this parameter space. The physical properties and the differences between the clumps of rotational variables are explored in Phillips et al. (in prep), but the spotted binaries in our catalog do not trace these clumps well.

We calculate rotation periods for the TESS light curves by manually masking the eclipses and running Lomb-Scargle periodograms (Lomb 1976; Scargle 1982) on the remaining light curves. In total, we compute rotation periods for 410 of the 426 binaries, excluding systems where the orbital/rotational period is long compared to the length of a TESS sector or systematics in the TESS light curve limit determination of the period. We find that the spotted binaries are almost all near tidal synchronization, which is expected for the short period systems in our sample (e.g., Lurie et al. 2017). Although we do observe some long-term modulations between TESS sectors (shown in Figure A1) that could be due to differential rotation (e.g., Reinhold et al. 2013), the gaps between the TESS sectors limit our ability to determine these modulation periods.

Three binaries have rotation to orbital period ratios  $|\log(P_{\text{rot}}/P_{\text{orb}})| > 0.05$ : Gaia DR3 5900431676207912448, 505860530871568512, and 1974523395151038208. Gaia DR3 5900431676207912448 is on the subgiant branch, and the rotation period of  $P_{\text{rot}} = 0.82$  days is about 1/5 of the orbital period of  $P_{\text{orb}} = 4.32$  days. The second target, Gaia DR3 505860530871568512, has  $\text{parallax\_over\_error} < 10$ , so we have no estimate of the evolutionary state. The periods of  $P_{\text{rot}} = 1.93$  days and  $P_{\text{orb}} = 2.92$  days are in a near 2:3 ratio. Finally, Gaia DR3 1974523395151038208 is on the upper main sequence ( $M_G \approx -1.2$  mag,  $G_{\text{BP}} - G_{\text{RP}} \approx -0.18$  mag) and the periods are  $P_{\text{rot}} = 3.89$  days and  $P_{\text{orb}} = 3.15$  days. This system has ATLAS  $r1 = 32''$ , and nearby variable stars in the ATLAS (J328.6176+46.9429) and ZTF (J215427.72+465633.8) catalogs, but neither have periods matching the rotation period.

Two targets, Gaia DR3 5201190414610275456 and 2191346572751253376, have  $G_{\text{BP}} - G_{\text{RP}} > 1.5$  mag after correcting for extinction. These systems are likely sub-sub giants, which are redder and fainter than typical giants/subgiants. Sub-subgiants are expected to form through mass transfer, envelope stripping, and/or magnetic fields (Mathieu et al. 2003). The orbital periods are 11.88 and 6.36 days, respectively, which are consistent with what is expected from a stripping interaction (Leiner et al. 2017). Gaia DR3 5201190414610275456 is also identified as an X-ray source in Chandra (Evans et al. 2010), XMM-Newton (Webb et al. 2020), and Swift (Evans et al. 2020). Both of these are promising targets for radial velocity followup to determine the masses and radii of sub-subgiants.



**Figure 4.** Gaia DR3 extinction-corrected color-magnitude diagram (CMD) colored by variability type. The solid lines show MIST isochrones for ages of  $10^8$  to  $10^{10}$  years in intervals of 0.5 dex. The flux is doubled in each band to represent binary stars of equal mass. The dashed lines show the boundaries of the giant and subgiant branches defined by R22. The five systems are significantly below the main sequence are discussed in Sections 3.3 and 3.7.

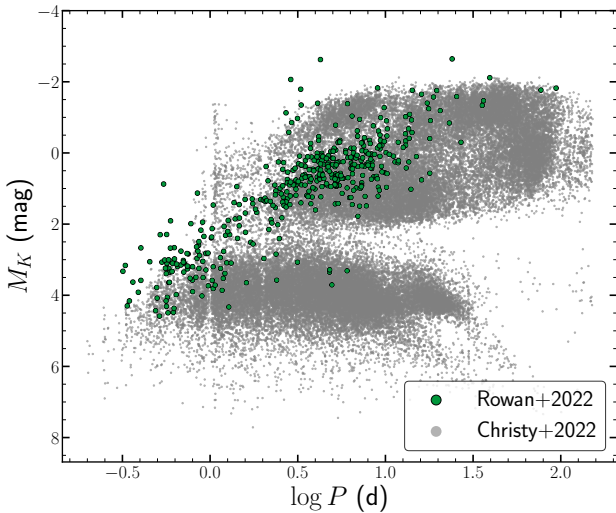


**Figure 5.** Distribution of  $M_K$  and orbital period for the rotational variables from the ASAS-SN  $g$ -band variables catalog (Christy et al. 2022) and the 426 targets in our catalog. Distinct clumps are found in the ASAS-SN  $g$ -band catalog, but the binaries in our catalog do not trace the clumps well.

### 3.2 Extra Eclipses

Unlike the spotted stars, which have a bimodal distribution of  $\log P$ , the distribution of  $\log P$  for the extra-eclipsing systems is unimodal with a median period of 3.35 days. Figure 2 shows that these systems are also more concentrated near the Galactic plane near the spotted stars, similar to the quadruple systems in Zasche et al. (2022). The extra-eclipsing systems are distributed across the main sequence, although they are typically of earlier types than the spotted stars. There are 46 systems with extra eclipses on the subgiant and red giant branches.

To determine the orbital period of the tertiary or second binary,  $P_2$ , we start by folding the ASAS-SN  $g$ -band and TESS light curves at the original orbital period,  $P_1$ . We then use the PHOEBE geometry estimator, which combines a two Gaussian model with a cosine term to estimate the orbital eccentricity, argument of periastron, and time of superior conjunction, to construct an analytic model. We try four different methods of subtraction/masking before searching for the second period:

- (i) Use the  $g$ -band analytic model to define the times of primary and secondary eclipse and mask out these times in the TESS light curve;
- (ii) Use the TESS analytic model to define and mask out times of primary and secondary eclipse;
- (iii) Subtract the analytic model from the TESS data; or

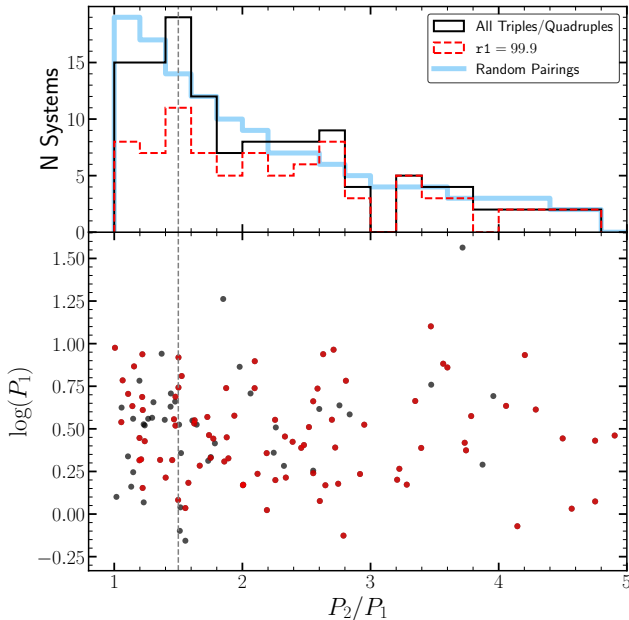


**Figure 6.** Orbital periods  $P_1$  and  $P_2$  for triple/quadruple systems. For the purposes of this figure,  $P_2$  is defined as the longer of the two orbital periods. Top: distribution of  $P_2/P_1$ . Systems with  $r_1 = 99.9$  are shown in red. Bottom: Distribution of  $P_2/P_1$  and  $\log(P_1)$ , showing there are some systems with period ratios exactly at 3:2.

(iv) Subtract the analytic model from the TESS data and mask out the eclipse

We then use the `astropy` implementation of the Box Least Squares (BLS) periodogram (Kovács et al. 2002; Astropy Collaboration et al. 2013) to determine  $P_2$ . We phase-fold the light curve at  $P_2$  and check that the period is reasonable and double the period when necessary. For some quadruple systems where the second binary is in contact, it is more effective to run a Generalized Least Squares (GLS) periodogram (Lomb 1976; Scargle 1982). While these four methods often produce the same  $P_2$ , there are some cases where one method is more effective. For instance, for light curves with non-flat out of eclipse shapes, methods (iii) and (iv) tend to be more effective because the periodogram power at the main binary orbital period is reduced. During this visual inspection process we also identify targets that require sigma-clipping due to TESS systematics before the period search is performed.

For systems where  $P_2$  is greater than the length of a TESS sector we are unable to calculate  $P_2$  if only one sector of data is available. There are also some systems where the systematics in the TESS light curve limit our ability to identify  $P_2$  even after clipping bad data points. Finally, there are a small number of systems where there are additional effects in the light curve, such as reflection, that are not represented by the analytic model. In total, we report values of  $P_2$  for 176 systems in Table 1.

Figure 6 shows the distribution of period ratios where  $P_2$  is defined to be the longer of the two periods. For comparison, we randomly pair the  $P$  and  $P_2$  orbital periods and show their distribution in period ratio as the blue line in Figure 6. There is a clear overabundance in systems near a period ratio of 3:2 in the sample, even when only including systems with  $r_1 = 99.9$ . Zasche et al. (2019) also identified an excess of systems at a 3:2 period ratio. The bottom panel of Figure

6 shows that these systems fall almost exactly at  $P_2/P_1 = 1.5$ , which is expected for orbital resonance.

However, we note that two of the binaries are apparent blends with each other. Gaia DR3 5618940344244565504 and Gaia DR3 5618940653482188160 are separated by  $\sim 60''$ , and both TESS light curves have eclipses with periods  $P_1 = 5.529231$  d and  $P_2 = 8.300885$  d, so  $P_2/P_1 = 1.5013$ .

We cross-match the systems with extra eclipses with catalogs of triples and doubly-eclipsing binaries from Zasche et al. (2019), Zasche et al. (2022), Borkovits et al. (2022), Kostov et al. (2022), Rappaport et al. (2022) and Table 1 of Borkovits et al. (2020). In total, 56 (25%) of our extra-eclipsing systems have been included in at least one of these catalogs<sup>2</sup>. Table 1 includes the citations for each binary. Out of these 56 systems, 7 have nearby variable stars listed in Table 2. One of these is CzeV343, which was discovered by Cagaš & Pejcha (2012) and studied in detail in Pejcha et al. (2022) and is clearly not a blend. The nearby variable star, ATLAS J087.1044+30.9502, is separated by  $13''.7$  and is listed as a dubious variable. The triple system TIC 52041148, is also returned in our cross-match to variables catalogs, and is unlikely to be a blend since it shows evidence of eclipse timing variations and eclipses of the tertiary in the ASAS-SN photometry (Borkovits et al. 2022). The remaining systems in the known triple/quadruple catalogs that have variable matches in Table 2 are in the Kostov et al. (2022) and Zasche et al. (2022) catalogs. Only one of these, TIC 251757935, has a variable star match to  $P_2$  in the ATLAS catalog, but the separation between the Gaia coordinates and the ATLAS variable is  $< 0''.1$ , suggesting that ATLAS has recovered the second orbital period and this is a true triple/quadruple system.

### 3.3 Reflection Effects

Mutual surface heating in close binary systems can alter the out-of-eclipse shape of the light curve. This reflection effect is generally more prominent for systems with shorter periods and large temperature differences. In our catalog, the median period of all 766 systems is 3.7 days, but the 29 reflection systems have a median period of 1.86 days. Of the 15 reflection systems with Gaia `parallax_over_error`  $> 10$  and  $A_V < 2.0$  mag, 10 have MS primaries and 5 have SG/RG primaries.

Three systems, Gaia DR3 6144569024718252544, 1375814952762454272, and 6652952415078798208 are much bluer than the binary main sequence with  $G_{BP} - G_{RP} \approx -0.4$  mag (see Figure 4). The first two have  $M_G \approx 4.1$  mag and  $P < 0.2$  days and are likely subdwarf B and M dwarf (sdB+dM) systems (e.g., Dai et al. 2022). Gaia DR3 6652952415078798208 is more luminous, with  $M_G = 2.3$  mag, and has a longer period of  $P = 0.36$  days, but it is likely also an sdB+dM binary, rather than an sdO+dM binary based on the color classification schemes given in Table 1 of Geier (2020).

This system also has additional scatter in the light curve that could be due to pulsations. We used the PHOEBE geometry estimator to mask the eclipses in the TESS light curve and then fit a sinusoid to subtract off the reflection effect signal. We use a Lomb-Scargle periodogram and find additional variability at  $P = 0.575455$  days with false-alarm probability  $< 10^{-7}$ . This frequency is lower than typically observed for pulsating sdB stars (Reed et al. 2014; Baran et al. 2019), so the nature of this variability is unclear.

<sup>2</sup> Two of the targets included in these catalogs were originally reported in Torres et al. (2017) and Cagaš & Pejcha (2012).



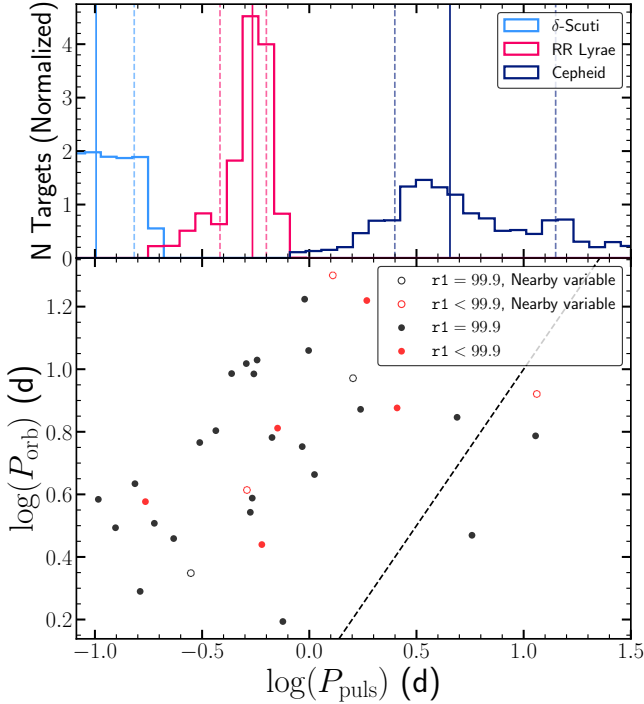


**Figure 7.** Pulsation periods for the 36 eclipsing systems with periodic pulsations. The top panel shows the normalized distribution of  $\delta$ -Scuti, RR Lyrae, and Cepheid variable periods from ASAS-SN with classification probabilities  $> 0.9$  from Jayasinghe et al. (2021). The vertical solid lines show the median  $\log P$  of the distributions and the dashed lines show the 16th and 84th quantiles of the distributions. Systems above the black line have pulsation periods longer than the orbital period. Systems with  $r1 < 36''$  are shown in red, and systems with nearby variable stars in Table 2 are shown as open circles.

Hot subdwarfs are likely to form through binary evolution with phases of common envelope evolution and Roche lobe overflow (e.g., Han et al. 2002), although single-star evolutionary channels (e.g., D’Cruz et al. 1996) and hierarchical triple models (e.g., Preece et al. 2022) have been proposed. Radial velocity followup of these targets can be used to characterize the masses and radii of both components and evaluate formation models.

### 3.4 Regular Pulsators

36 systems have additional periodic variability in their light curves that is due to pulsations rather than extra eclipses. We use the procedures described in Section 3.2, substituting the Generalized Lomb Scargle periodogram (Lomb 1976; Scargle 1982) rather than a BLS, to calculate the period. We are able to calculate the pulsation period for all but 2 systems, and report the pulsation periods in Table 1. Figure 7 shows the distribution of pulsation and orbital periods compared to the distribution of pulsational variables in Jayasinghe et al. (2021).

The majority of targets have  $\delta$ -Scuti, RR Lyrae, or Cepheid-like pulsations. We identify four systems with Cepheid pulsations: Gaia DR3 6140491142248459776 ( $P_{\text{orb}} = 2.95$  d), 2070234748476679424 ( $P_{\text{orb}} = 9.36$  d), 2952256516644702720 ( $P_{\text{orb}} = 7.02$  d), and 5350308140079159168 ( $P_{\text{orb}} = 16.58$  d). The smallest Cepheids are expected to have radii  $\sim 30 R_{\odot}$  (Gieren et al. 1999) and masses  $3\text{--}5 M_{\odot}$ . Even if the companion was a

low-mass main sequence star, which is unlikely given the relative eclipse depths, the orbital period based on Kepler’s third law must be  $\gtrsim 10$  days. Since these systems are detached with minimal ellipsoidal effects in the light curves, the periods would have to be even larger, suggesting these targets are blends. However, only one of these targets, Gaia DR3 5350308140079159168, has  $r1 = 29''8$ .

Of these four systems, only Gaia DR3 2070234748476679424 with  $P_{\text{puls}} = 1.6$  days has nearby variable stars in the ZTF and ATLAS catalogs. ZTF J204433.65+452440.5 is separated by  $16''.7$ , has a  $g$ -band period of 0.87 days, and is classified as an RS CVn (Chen et al. 2020). We downloaded and phase-folded the ZTF light curve at our derived  $P_{\text{puls}}$  and do not find pulsational variability consistent with the TESS period. The ATLAS variables catalog (Heinze et al. 2018) includes J311.1366+45.4141, which is separated by  $17''.2$ . The Lomb-Scargle period is 0.39 days, and the system is listed as a “dubious” variable. This system must be a blend given the orbital period and the typical radii of Cepheids, but nearby matches to variable catalogs do not contain systems with the expected period.

Gaia DR3 6727189722220410752 and 3028351483024584832 are apparent RR Lyrae eclipsing binaries with ATLAS  $r1 = 99.9$ . Neither of these targets have nearby variable stars  $< 21''$  in the Gaia, ATLAS, ZTF, or ASAS-SN variable star catalogs. We classify the later system as a first overtone RR Lyrae (RRC) because of the short pulsation period  $P_{\text{puls}} = 0.31$  days and the nearly sinusoidal nature of the light curve. Neither of the ASAS-SN light curves of these targets shows similar pulsational variability at these periods.

We expanded the search radius from  $21''$  to  $60''$  and repeated the cross match for both targets. For Gaia DR3 6727189722220410752, we find an RR Lyrae separated by  $57''.1$  in the ASAS-SN  $V$ -band catalog (Jayasinghe et al. 2021) with the same pulsation period  $P_{\text{puls}} = 0.57$  days that we recovered from the TESS light curve. We find no nearby contaminating variable stars within  $1'$  for 3028351483024584832, so we further extend the search radius to  $3'$ . We find no matches in the ASAS-SN variable catalog, but identify ZTF J073112.04-152905.2, separated by  $2''.8$ . Chen et al. (2020) identified this system as a contact binary with a period of 0.32 days, which is consistent with our derived pulsation period. The amplitude of the variability in the TESS light curve is small ( $\sim 0.025$  mag). However, ZTF J073112.04-152905.2 is  $g \sim 17.59$  mag and Chen et al. (2020) reports an amplitude  $\Delta g = 0.452$  mag.

Whether this system is best classified as a contact binary or a pulsator, it is likely that the extra variability in the TESS light curve of 3028351483024584832 is due to a blended variable. Both of these variables demonstrate the wide separations where blending from variable stars with high amplitudes can contaminate TESS light curves.

We find two targets that we label as  $\beta$ -Cephei pulsations. Gaia DR3 3123204972458091008 is in a  $P_{\text{orb}} = 6.05$  day binary with a pulsation period of  $P_{\text{puls}} = 0.67$  days. Gaia DR3 5310247781838683648 is in a  $P_{\text{orb}} = 1.56$  day binary and has a pulsation period of  $P_{\text{puls}} = 0.75$  days. Both targets are found on the upper main sequence and are consistent with A or B type primaries. The pulsations of Gaia DR3 3123204972458091008 are highly regular both in their arrival time and amplitude, and are similar to those of  $\eta$  Ori (Southworth & Bowman 2022, Figure 1) although only one Sector of TESS data is available. The binary itself is also eccentric,  $e > 0.2$  based on the PHOEBE geometry estimator fit. On the other hand, the Gaia DR3 5310247781838683648 pulsations change in amplitude across the single Sector of available TESS data and are more similar to 16 Lac (Southworth & Bowman 2022). Both of these binaries are promising targets for asteroseismic modeling with additional constraints from spectroscopic orbit results. Such systems can be used to validate and

**Table 3.** Pulsation frequencies for the 17 eclipsing  $\gamma$ -Dor variable candidates.

Gaia DR3	$\nu_{\text{orb}}$ (1/d)	$\nu_1$ (1/d)	$\nu_2$ (1/d)	$\nu_3$ (1/d)	$\nu_4$ (1/d)	$\nu_5$ (1/d)
5808714298849592192	0.519	1.266	1.130	0.228	2.306	2.169
443999635867486720	0.518	1.180	1.053	1.443	1.310	
5331653898816403584	0.442	0.880	0.719	0.953	0.561	0.599
248169674294594816	0.381	0.914	0.977	0.816	0.764	1.058
434846854403757184	0.289	0.858	0.703	0.798	0.644	0.284
263700752773032448	0.255	1.147	1.211	1.058	0.737	1.544
1999637031003866368	0.244	1.478	1.710	1.544	1.649	1.815
5693600963342153088	0.220	0.440	0.872	0.807	0.384	0.609
351850661555541504	0.191	0.647	0.588	1.084	0.707	0.528
5248678051242539136	0.188	0.712	0.491	0.546	0.460	0.637
3103470323585557376	0.185	0.609	0.787	0.675	0.971	
23092256739885312	0.176	0.600	0.663	0.498	0.553	1.167
4532112201568025728	0.169	0.554	0.507	0.986	0.934	0.432
3143993576241783040	0.159	1.547	1.214	0.643	0.763	0.234
3249778590678600448	0.126	0.377	0.484	0.435	0.628	0.317
5288047130219214080	0.122	0.527	0.365	0.464	0.418	0.386
435896716209335040	0.121	1.039	1.235			

improve interior structure models for massive stars and the impact of close binary companions (e.g. [Soydugan et al. 2006a](#); [Schmid & Aerts 2016](#); [Tkachenko et al. 2020](#)).

### 3.5 Stochastic Variability

We identify 24 targets with stochastic variability in their light curves. These were identified and distinguished from the regular pulsators and  $\gamma$ -Dor pulsators by inspecting the unfolded TESS light curves. The variability has typical timescales of hours to days, and is consistent with the stochastic low frequency variability that arises from from turbulent core convection driven gravity waves in massive stars ([Bowman et al. 2019, 2020](#); [Southworth & Bowman 2022](#)). Figure A2 shows examples of their TESS light curves.

We only report the evolutionary state for 10 of these targets. The rest have extinction  $A_V > 2.0$  (7 systems), Gaia `parallax_over_error` < 10 (6 systems) or both (1 system). Of the systems with reported evolutionary states, 7 have absolute magnitudes consistent with OBA MS stars. One system, Gaia DR3 5560556684818159872, is on the giant branch, which might indicate a different origin of variability compared to the rest of the targets.

### 3.6 $\gamma$ -Dor Pulsators

We identify 17 systems with  $\gamma$ -Dor pulsations, all of which are near  $G_{\text{BP}} - G_{\text{RP}} \sim 0.5$  mag and  $M_G \sim 2.5$  mag on the CMD (Figure 4) as expected from catalogs of  $\gamma$ -Dor pulsators (e.g., [Li et al. 2020](#)). All of the  $\gamma$ -Dor systems except for Gaia DR3 5331653898816403584 have ATLAS `r1` = 99.9 and all have orbital periods  $P < 10$  days (Figure 3). Since many of these systems have multiple frequency components and the amplitudes of the pulsations change over the course of a single binary orbit, we separated them from the regular pulsators. We perform a similar period search as for the regular pulsators described in Section 3.4, but identify multiple frequencies for most of our targets above a false alarm level of  $10^{-5}$ . We also only considered pulsation periods shorter than 5 days based on typical periods for  $\gamma$ -Dor pulsators (e.g., [Henry et al. 2011](#)).

Figure 8 shows an example periodogram and light curves for Gaia DR3 263700752773032448. The top panel shows the Lomb-Scargle periodogram where the highest-power frequencies are not consistent

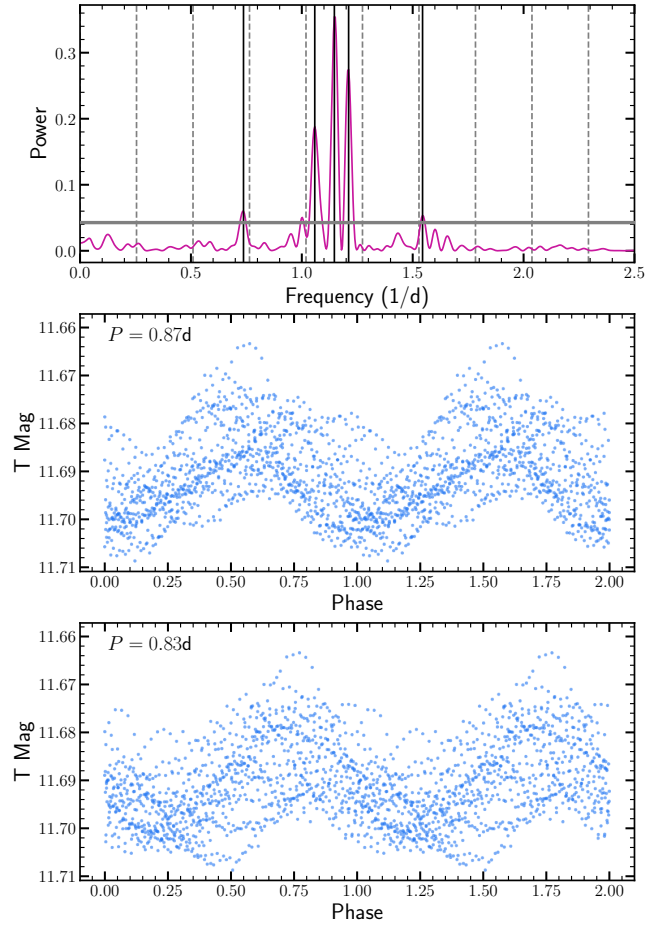


**Figure 8.** Example of a frequency search for the  $\gamma$ -Dor eclipsing candidate Gaia DR3 263700752773032448. Top: the Lomb-Scargle periodogram after masking the eclipses. The vertical dashed gray lines show harmonics of the orbital frequency, and the solid lines show the five frequencies reported in Table 3. The horizontal gray line shows the false alarm level of  $10^{-5}$ . Middle: the TESS light curve folded at the frequency with the highest power. Bottom: the TESS light curve folded at the frequency with the second highest power.

with harmonics of the orbital frequency (gray dashed lines). The bottom two panels show the TESS light curve folded at the two best frequencies. In total, we detect six significant pulsation frequencies for this target. Table 3 reports the five best pulsation frequencies for all targets. Since  $\gamma$ -Dor pulsations are gravity-mode, or g-mode, pulsations ([Kaye et al. 1999](#)), they can be used to study the interior structures of stars ([Van Reeth et al. 2016](#)) with additional constraints from the masses and radii based on the eclipses (e.g., [Southworth & Van Reeth 2022](#)).

### 3.7 Other Targets

There are 9 systems that do not fit into these categories and are shown in Figure 9. Here we briefly describe their properties and offer possible classifications.

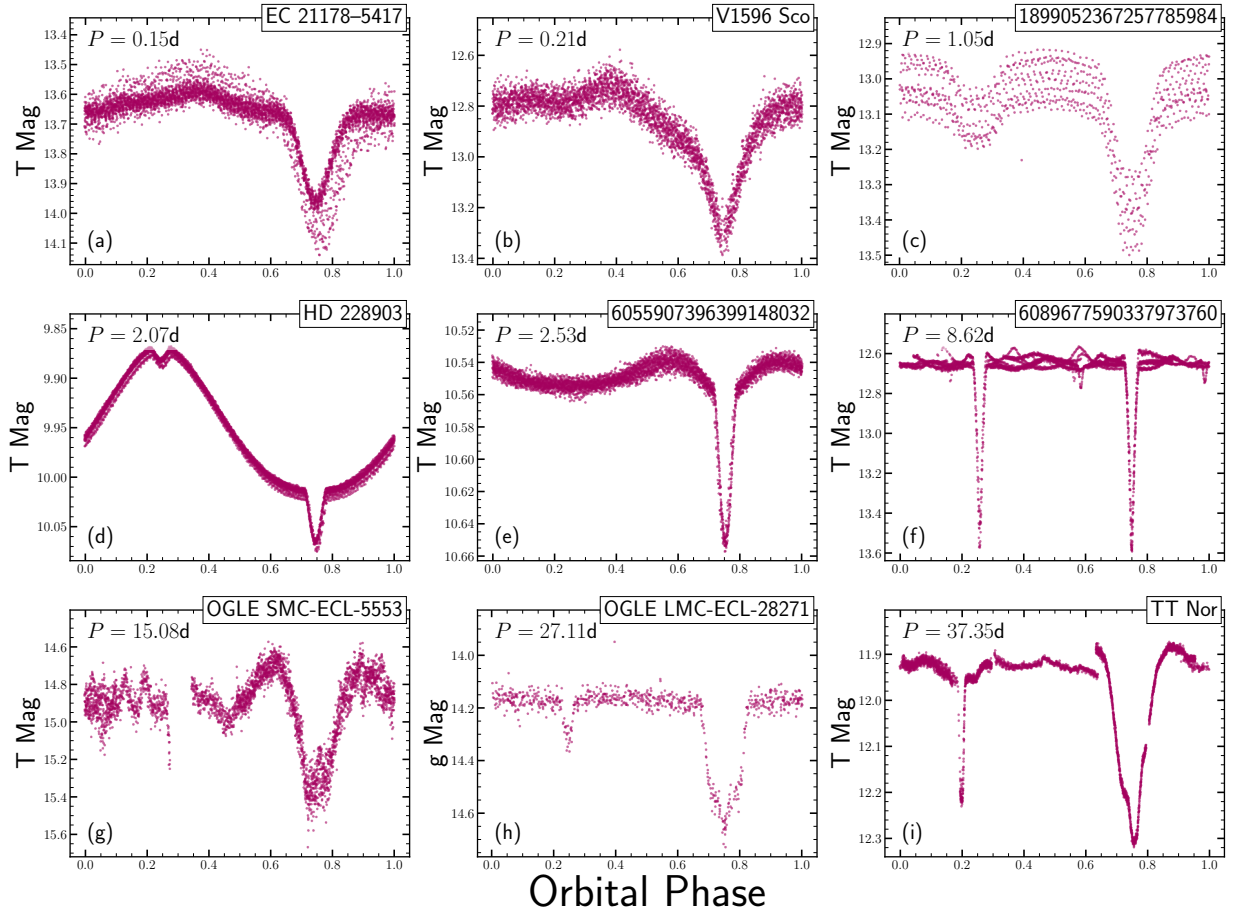


**Figure 9.** Same as Figure 1, but for systems that do not fit into one of the main classifications. The properties of these systems are described in Section 3.7. The Gaia DR3 source or other identifier are reported in the top right of each panel.

### 3.7.1 White Dwarf+MS Disk Systems

Gaia DR3 6463668670854493952 (EC 21178–5417, Figure 9a) and 6031156290142441344 (V1596 Sco, Figure 9b) are found between the white dwarf cooling sequence and the main sequence on the CMD (Figure 4). Both have orbital short orbital periods,  $P = 0.15$  and  $P = 0.21$  days, respectively. The light curves show a single eclipse deep eclipse with asymmetric ingress and egress shapes.

EC 21178–5417 is found in a number of CV catalogs (Stobie et al. 1997; Downes et al. 2001; Ritter & Kolb 2003; Ak et al. 2008) and is typically classified as a nova-like variable. Photometric observations of this system have identified quasi-periodic oscillations (QPOs) and dwarf-nova oscillations (DNOs, Warner et al. 2003) in addition to the eclipses. Spectroscopic observations identified double-peaked HeII emission lines, suggesting an inclined accretion disk (Khangale et al. 2020).

We did not find V1596 Sco in any CV catalogs, but the system is likely also a nova-like variable based on the similarities to EC 21178–5417. V1596 Sco was included in the Shi et al. (2022) catalog of pulsating eclipsing sources in TESS. We mask the eclipses in the TESS data and recover variability at the same period of  $P = 0.0513$  days. This period is about a factor of 10 longer than the QPOs and more than 100 times longer than the DNOs identified in EC 21178–5417 by

Warner et al. (2003), and further observations are needed to identify the origin of this variability.

### 3.7.2 Ellipsoidal triple

Gaia DR3 1899052367257785984 (Figure 9c) is in a 1.05353 day orbit detected in ASAS-SN (Jayasinghe et al. 2021), ZTF (Chen et al. 2020), and ATLAS (Heinze et al. 2018). The TESS light curve shows additional variability at 9.09 days that is consistent with ellipsoidal modulations. The amplitude of this variability is about half of the amplitude of the primary eclipse, but no variability is seen in the ASAS-SN, ZTF, or ATLAS light curves. ATLAS reports an  $r1 = 16''8$ , suggesting this target is likely a blend.

### 3.7.3 Eclipsing Subdwarf

Gaia DR3 2068355163403333504 (HD 228903) has a light curve consistent with eclipsing subdwarfs (e.g., Østensen et al. 2010) and shows a strong reflection effect in addition to shallow, short duration eclipses evenly spaced in orbital phase (Figure 9d). The orbital period,  $P = 2.07231$  days is about  $\sim 1/4$  of the period reported in the ASAS-SN variable stars catalog (Jayasinghe et al. 2021), and this target is not included in the ZTF or ATLAS variability catalogs,

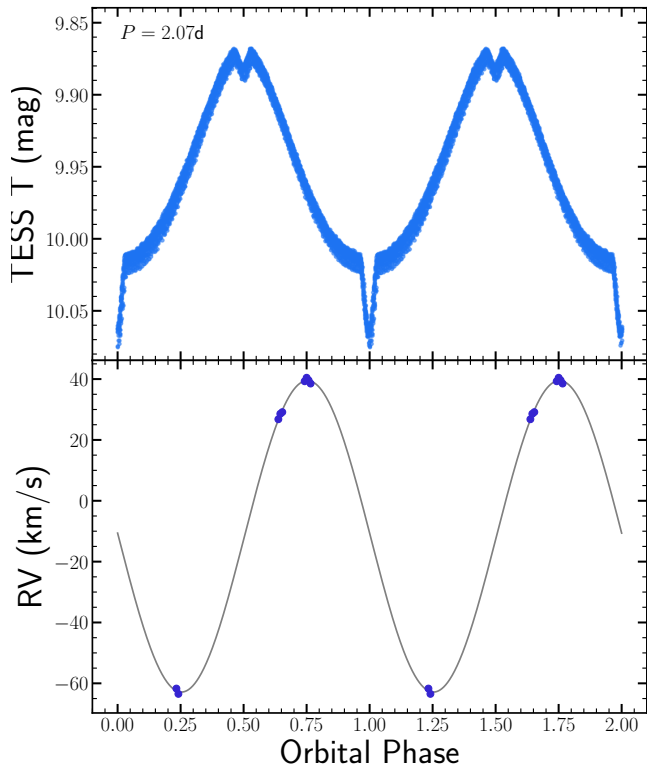


**Figure 10.** Light curve and LAMOST radial velocity curve of HD 228903, an eclipsing subdwarf system, phased such that the deeper eclipse is at phase 0.0. The gray line shows a circular orbit fit to the RV data.

despite being in the northern hemisphere. This system was identified in the WISE catalog of variable stars with a period of 4.1443471 days in the miscellaneous category (Chen et al. 2018). The WISE W1 and W2 light curves both show the reflection effect, but the eclipses are not visible. On the CMD, this target appears near the upper main sequence ( $M_G \approx -0.4$  mag,  $G_{BP} - G_{RP} \approx 0.3$  mag) but it is likely evolving along the horizontal branch given the large temperature difference and similarities to subdwarf binaries and HW Virginis systems. HD 228903 has been detected as an X-ray source by XMM-Newton (Traulsen et al. 2020) and as UV source by Swift (Yershov 2014).

HD 228903 was identified as a spectroscopic binary in the Large sky Area Multi-Object fiber Spectroscopic Telescope (LAMOST, Cui et al. 2012) medium resolution survey (MRS, Zhang et al. 2022) and nine radial velocity measurements are available. We use the photometric period and ephemeris to phase the radial velocity data as shown in Figure 10. Since the light curve suggests a circular orbit, we fixed the eccentricity to zero and found a velocity semi-amplitude of  $K = 51.2 \pm 0.4$  km/s and a mass function of  $f(M) = 0.029 M_\odot$ . As expected, the maximum radial velocity occurs at phase 0.75.

### 3.7.4 Eccentric inclined system

Gaia DR3 6055907396399148032 is a main sequence binary with an orbital period of  $P = 2.53314$  days. The light curve (Figure 9e) shows a single deep eclipse with a parabolic out of eclipse shape. Since the light curve maxima occur immediately before and after the eclipse, this system is probably in a inclined eccentric orbit without a

secondary eclipse. We use emcee (Foreman-Mackey et al. 2013) and PHOEBE (Prša & Zwitter 2005; Prša et al. 2016; Conroy et al. 2020) to fit the TESS light curve. To reduce computation time, we use only every tenth point in the TESS light curve. We start by following the optimization procedure described in R22, and then run the MCMC chain for 50000 iterations with a 3000 iteration burn in period. Figure 11 shows the light curve sampled from the MCMC posteriors and the distributions of eccentricity and inclination. The estimated eccentricity and inclination are  $e = 0.130 \pm 0.002$  and  $i = 67.9 \pm 0.1^\circ$ . The tidal distortion near periastron provides the constraints on the inclination and eccentricity. However, similar systems observed with lower photometric precision may be incorrectly assumed to be at twice the period and in a circular orbit. Radial velocity observations of this system can confirm the orbital period.

### 3.7.5 Extra-Eclipsing $\gamma$ -Dor system

Gaia DR3 6089677590337973760 shows additional eclipses and  $\gamma$ -Dor-like pulsations (Figure 9f). We start by masking the deeper eclipses and identify a periodicity near  $\sim 24.2$  days corresponding to the additional pair of eclipses. Since data is only available for two TESS sectors, additional observations are needed to validate and further constrain this period. We then mask out the second pair of eclipses and use a Lomb-Scargle periodogram to identify the pulsation frequencies. The three dominant frequencies are at  $\nu_1 = 0.578$ ,  $\nu_2 = 0.430$ , and  $\nu_3 = 0.481$  d $^{-1}$ . ATLAS reports  $r1 = 4''.9$ , but this target has declination  $DEC = -51.1^\circ$ , so it is outside the footprint of the ATLAS and ZTF variable catalogs. However, the  $G = 12.8$  mag variable Gaia DR3 6089677586043502848 is classified as an eclipsing binary with a period of  $P = 1.5256$  days. If Gaia DR3 6089677586043502848 is the blended target producing additional eclipses, the incorrect period in the Gaia catalog may come from the few epochs of observation available in the Gaia photometry.

To determine which eclipsing binary is more likely to have the  $\gamma$ -Dor pulsating component, we can consider their CMD positions. Gaia DR3 6089677590337973760 has absolute magnitude and color  $M_G \approx 3.6$  mag,  $G_{BP} - G_{RP} \approx 0.65$  mag. This is slightly fainter and redder than the majority of  $\gamma$ -Dor pulsators (e.g. Figure 3 of Sepulveda et al. 2022). The blended eclipsing binary, Gaia DR3 6089677586043502848 has absolute magnitude and color  $M_G \approx 1.6$  mag,  $G_{BP} - G_{RP} \approx 0.35$  mag, which is brighter than the  $\gamma$ -Dor pulsators in our catalog (Figure 4), but is consistent with the brightest  $\gamma$ -Dor pulsators in the Li et al. (2020) catalog. The nearby binary Gaia DR3 6089677586043502848 is therefore more likely to host the  $\gamma$ -Dor pulsator.

### 3.7.6 Eclipsing heartbeat star in the SMC

Gaia DR3 4687138015328580736 (OGLE SMC-ECL-5553, Figure 9g) appears to be an eclipsing heartbeat star in the SMC identified as an eclipsing binary in the Optical Gravitational Lensing Experiment (Udalski et al. 1992; Pawlak et al. 2013, OGLE). Heartbeat stars are a rare class of variable stars (Thompson et al. 2012; Jayasinghe et al. 2019b; Wrona et al. 2022), showing tidal distortions near pericenter and tidally-excited oscillations (TEOs, Fuller 2017). These stars can be used to empirically study the tidal interactions within binary stars (e.g., Beck et al. 2018).

OGLE SMC-ECL-5553 has also been identified as an X-ray source in XMM-Newton (Page et al. 2012) and an infrared variable in the Spitzer SAGE-SMC survey (Gordon et al. 2011; Polsdofer et al. 2015). No TESS light curve is available through the QLP or SPOC

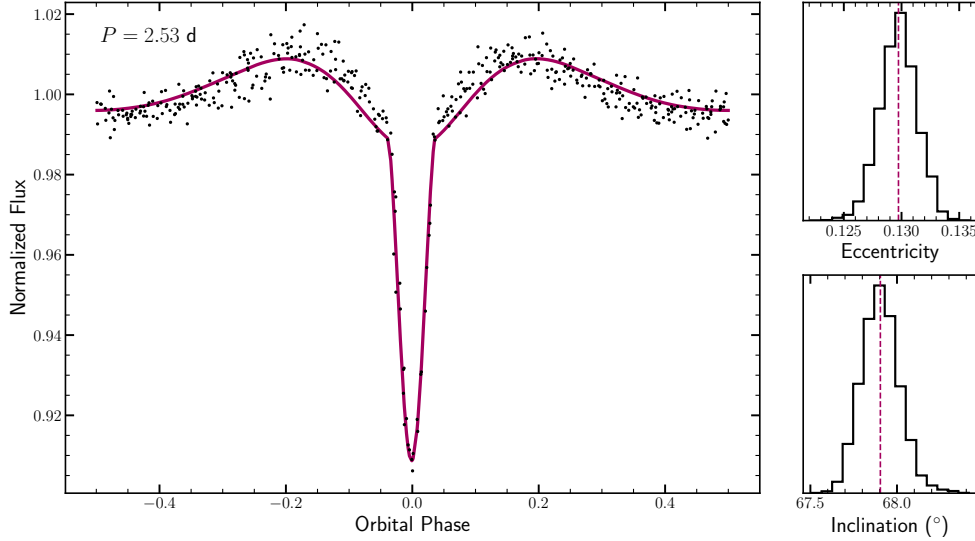


**Figure 11.** TESS light curve of Gaia DR3 6055907396399148032 and the MCMC posteriors for the eccentricity and inclination. The geometry of this system prevents detection of a secondary eclipse, so the system geometry is determined from the distortions near the primary eclipse.

pipelines, so we extracted a light curve from the sector 27 full-frame images using *eleanor*. In addition to showing the clear eclipses and brightening between eclipses, the TESS light curves shows additional TEOs with a period of  $P_{\text{TEO}} \approx 1.2$  days. This variability is not seen in the OGLE light curve, which may indicate it comes from a nearby variable star. Since this target is in the SMC, it is outside the footprint of the ALTAS and ZTF variable catalogs but we find no contaminating variables matching the period of the oscillations in the ASAS-SN or OGLE catalogs (Soszyński et al. 2010, 2011; Pawlak et al. 2013; Soszyński et al. 2015; Pawlak et al. 2016), so the origin of this variability is unclear.

### 3.7.7 Disk Eclipping Systems

The two systems in the “other” category that have the longest orbital period are Gaia DR3 4655260836825948160 (OGLE LMC-ECL-28271) and Gaia DR3 5884699932561933696 (TT Nor) with periods  $P = 27.1$  d and  $P = 37.4$  d, respectively. Both show two eclipses with dramatically different widths and unusual primary eclipse shapes (Figure 9h and 9i). In the case of OGLE-LMC-ECL-28271, the primary eclipses last  $\sim 0.14$  in orbital phase, which is  $\sim 3.8$  days. In the middle of the primary eclipse, an additional eclipse occurs. The secondary eclipse, separated by 0.5 in orbital phase, is much narrower and shallower and is more consistent with the additional eclipsing feature seen in the primary eclipse. This system was labeled as an eclipsing binary in OGLE (Pawlak et al. 2013), and the OGLE I-band light curve shows the same eclipse features as the ASAS-SN light curve.

TT Nor also shows two eclipses of extremely different widths and an asymmetric primary eclipse, but here the additional dip in the primary eclipse occurs just before egress. The system is also eccentric, which likely partially contributes to the unequal eclipse widths. Although the orbital period is longer than a TESS sector, two sectors of TESS data are available and provide full orbital phase coverage. Unlike OGLE-LMC-ECL-28271, the secondary eclipse does not resemble the extra ‘dip’ in the primary eclipse. The differences between these two systems could be due to differences in disk size and inclination.

## 4 DISCUSSION

We present a catalog of eclipsing binaries with additional features in their light curves due to spots, additional eclipsing companions, pulsations, and reflection effects. These binaries were identified through visual inspection of TESS and ASAS-SN light curves in R22. Table 1 gives the parameters of each system and Table 2 provides possible blended targets. The full table is available at <https://asas-sn.osu.edu/binaries> and in the electronic version of the paper. Table 4 summarizes the results for each group. After grouping the targets by the nature of the extra-physics observed in their light curves, we explore the parameters of each group.

For spotted stars (Section §3.1), we find the distribution of orbital period is closely tied to evolutionary state (Figure 3), and few spotted targets are identified on the upper main sequence. Many of these targets are chromospherically active X-ray sources. We also identify two red ( $G_{\text{BP}} - G_{\text{RP}} > 1.5$  mag) sub-subgiant candidates. Spectroscopic followup of these systems could be used to determine dynamical masses and radii, which could inform formation and evolutionary pathways (Geller et al. 2017; Leiner et al. 2017).

Our catalog contains 225 targets with extra-eclipses that suggest a hierarchical triple/doubly eclipsing binary configuration (Section §3.2). However, this group has the largest number of targets with nearby variables and proximity statistic  $r1 < 36''$  (Table 4), suggesting that some are likely blends of variables due to the low resolution of TESS. Similar to Zasche et al. (2019), we identify an excess of systems with 3:2 period resonance (Figure 6), which is unlikely to occur from random pairings or blended sources. The detection and characterization of hierarchical triple systems can be used to study dynamical processes such as Kozai cycles and tidal friction that impact the evolution of the period and eccentricity of the inner binary (Mazeh & Shaham 1979). Similar dynamical effects occur for quadruple systems made up of two pairs of binaries (Pejcha et al. 2013). For example, CzeV343, which is included in our catalog and was originally identified by Cagaš & Pejcha (2012), is a quadruple system with orbital periods in a near 3:2 ratio. Pejcha et al. (2022) determined the period and eccentricity of the mutual orbit and confirmed they are bound. The characterization of such systems are relevant to developing models of resonant capture (Tremaine 2020).

**Table 4.** Summary of group parameters. The “N TESS” column reports the number of systems where TESS QLP or SPOC light curves are available. the  $P_2$  column reports the number of systems where pulsation/orbital periods could be estimated. The “N Blend” column gives the number of binaries where a nearby variable is found in the Gaia, ATLAS, or ZTF catalogs (Table 2). The  $r1 < 36''$  column reports the number of systems where ATLAS reports a distance where the cumulative flux of nearby stars equals the target. The number of targets with X-ray detections are given in the X-ray column, and the MS, SG, RG columns give the evolutionary state of the primary based on the MIST isochrone/evolutionary track divisions.

Group	Total	N TESS	N $P_2$	N Blend	$r1 < 36''$	N X-ray	MS	SG	RG
Spotted Stars	426	398	410	34 (8.0%)	45 (10.6%)	68	127	177	105
Triples/Quads	225	225	176	54 (24.0%)	69 (30.7%)	2	126	33	13
Reg. Pulsator	36	36	34	5 (13.9%)	8 (22.2%)	1	22	4	0
Reflection	29	27	4	13.8%	20.7%	2	10	2	3
Stochastic Var.	24	24	5	20.8%	20.8%	0	4	5	1
$\gamma$ -Dor Pulsator	17	17	2	11.8%	05.9%	0	17	0	0
Other	9	7	4	44.4%	44.4%	1	6	0	0

We perform a similar period calculation procedure for the regular pulsators and  $\gamma$ -Dor systems (Sections §3.4 and §3.6), identifying multiple significant frequencies for the later group. Most, if not all, of the Cepheid and RR Lyrae pulsators appear to be blends, highlighting the need for additional photometry to confirm these systems. Systems with  $\delta$ -Scuti,  $\gamma$ -Dor, and  $\beta$ -Cephei pulsations may be used to place additional constraints on stellar parameters and improve understanding of stellar interiors (e.g., Johnston et al. 2019). We also find 24 binaries with stochastic low frequency variability (Section §3.5), which likely arises from gravity waves in massive stars (Bowman et al. 2019). Spectroscopic followup of these systems could be used to derive dynamical masses and make direct comparisons with asteroseismic models, improving our understanding of stellar interiors.

Finally, we investigate 9 systems that don’t fit into these groups (Section §3.7). We highlight two eclipsing CVs, two disk systems, a heartbeat star, and an eclipsing subdwarf. Four of these systems could be considered possible blends based on crossmatches to variable star catalogs or the  $r1$  proximity statistic (Table 4). We identify two systems, Gaia DR3 899052367257785984 (Section §3.7.2) and Gaia DR3 6089677590337973760 (Section §3.7.5) as clear blends. EC 21178–5417 is unlikely to be a blend given the CMD position and previous detailed studies. The disk eclipsing variability seen in OGLE LMC–ECL–28271 is observed by both ASAS-SN and OGLE, making this system also unlikely to be a blend. Characterization of these exotic systems can be used to study unique stages of binary evolution (e.g., Østensen et al. 2010; Khangale et al. 2020).

It is clear, however, that the low resolution of TESS makes the blending of distinct variables a considerable problem. Additional photometric and spectroscopic observations of these targets can be used to confirm the nature of the variability and derive dynamical masses and radii. All of the systems reported in this catalog were identified as eclipsing binaries in ASAS-SN Jayasinghe et al. (2021), and many of the ASAS-SN light curves are clear outliers from standard eclipsing binaries. The complementary nature of the long-baseline, daily cadence ASAS-SN light curves and the short duration, high precision TESS photometry allows for accurate identification and characterization of the “extra-physics” in these systems.

## ACKNOWLEDGEMENTS

We thank JJ Hermes for his valuable comments and discussion. We thank Las Cumbres Observatory and its staff for their continued support of ASAS-SN. ASAS-SN is funded in part by the Gordon and Betty Moore Foundation through grants GBMF5490 and

GBMF10501 to the Ohio State University, and also funded in part by the Alfred P. Sloan Foundation grant G-2021-14192.

DMR, TJ, KZS and CSK are supported by NSF grants AST-1814440 and AST-1908570. Support for TJ was provided by NASA through the NASA Hubble Fellowship grant HF2-51509 awarded by the Space Telescope Science Institute, which is operated by the Association of Universities for Research in Astronomy, Inc., for NASA, under contract NAS5-26555.

This work has made use of data from the European Space Agency (ESA) mission *Gaia* (<https://www.cosmos.esa.int/gaia>), processed by the *Gaia* Data Processing and Analysis Consortium.

This paper includes data collected with the *TESS* mission, obtained from the MAST data archive at the Space Telescope Science Institute (STScI). Funding for the *TESS* mission is provided by the NASA Explorer Program. STScI is operated by the Association of Universities for Research in Astronomy, Inc., under NASA contract NAS 5-26555. CSK, KZS and DMR *TESS* research is supported by NASA grant 80NSSC22K0128.

## DATA AVAILABILITY

The ASAS-SN photometric data underlying this article are available in the ASAS-SN eclipsing binaries database (<https://asas-sn.osu.edu/binaries>) and the ASAS-SN Photometry Database (<https://asas-sn.osu.edu/photometry>). The data underlying this article are available in the article and in its online supplementary material.

## REFERENCES

- Ak T., Bilir S., Ak S., Eker Z., 2008, *New Astron.*, **13**, 133  
 Andersen J., 1991, *A&ARv*, **3**, 91  
 Astropy Collaboration et al., 2013, *A&A*, **558**, A33  
 Bailer-Jones C. A. L., Rybizki J., Foesneau M., Demleitner M., Andrae R., 2021, *VizieR Online Data Catalog*, p. I/352  
 Baran A. S., Telting J. H., Jeffery C. S., Østensen R. H., Vos J., Reed M. D., VĀcković M., 2019, *MNRAS*, **489**, 1556  
 Beck P. G., Mathis S., Gallet F., Charbonnel C., Benbakoura M., García R. A., do Nascimento J. D., 2018, *MNRAS*, **479**, L123  
 Borkovits T., Rappaport S., Hajdu T., Sztakovics J., 2015, *MNRAS*, **448**, 946  
 Borkovits T., et al., 2020, *MNRAS*, **496**, 4624  
 Borkovits T., et al., 2022, *MNRAS*, **510**, 1352  
 Bovy J., Rix H.-W., Green G. M., Schlafly E. F., Finkbeiner D. P., 2016, *ApJ*, **818**, 130  
 Bowman D. M., et al., 2019, *A&A*, **621**, A135  
 Bowman D. M., Burssens S., Simón-Díaz S., Edelmann P. V. F., Rogers T. M., Horst L., Röpke F. K., Aerts C., 2020, *A&A*, **640**, A36

- Cagaš P., Pejcha O., 2012, *A&A*, **544**, L3
- Caldwell D. A., et al., 2020, *Research Notes of the American Astronomical Society*, **4**, 201
- Chen X., Wang S., Deng L., de Grijs R., Yang M., 2018, *ApJS*, **237**, 28
- Chen X., Wang S., Deng L., de Grijs R., Yang M., Tian H., 2020, *ApJS*, **249**, 18
- Choi J., Dotter A., Conroy C., Cantiello M., Paxton B., Johnson B. D., 2016, *ApJ*, **823**, 102
- Christy C. T., et al., 2022, arXiv e-prints, p. arXiv:2205.02239
- Conroy K. E., et al., 2020, *ApJS*, **250**, 34
- Cui X.-Q., et al., 2012, *Research in Astronomy and Astrophysics*, **12**, 1197
- D’Cruz N. L., Dorman B., Rood R. T., O’Connell R. W., 1996, *ApJ*, **466**, 359
- Dai M., Chen X.-D., Wang K., Luo Y.-P., Wang S., Deng L.-C., 2022, *Research in Astronomy and Astrophysics*, **22**, 035022
- Damiani C., Maceroni C., Cardini D., Debusscher J., Balaguer-Núñez L., Ribas I., 2010, *Ap&SS*, **328**, 91
- Davenport J. R. A., Windemuth D., Warmbein K., Howard E. L., Klein C., Birky J., 2021, *AJ*, **162**, 189
- Dotter A., 2016, *ApJS*, **222**, 8
- Downes R. A., Webbink R. F., Shara M. M., Ritter H., Kolb U., Duerbeck H. W., 2001, *PASP*, **113**, 764
- Drimmel R., Cabrera-Lavers A., López-Corredoira M., 2003, *A&A*, **409**, 205
- Evans I. N., et al., 2010, *ApJS*, **189**, 37
- Evans P. A., et al., 2020, *ApJS*, **247**, 54
- Foreman-Mackey D., Hogg D. W., Lang D., Goodman J., 2013, *PASP*, **125**, 306
- Fuller J., 2017, *MNRAS*, **472**, 1538
- Gaia Collaboration et al., 2022, arXiv e-prints, p. arXiv:2208.00211
- Geier S., 2020, *A&A*, **635**, A193
- Geller A. M., et al., 2017, *ApJ*, **840**, 66
- Gieren W. P., Moffett T. J., Barnes Thomas G. I., 1999, *ApJ*, **512**, 553
- Gieren W., et al., 2015, *ApJ*, **815**, 28
- Gordon K. D., et al., 2011, *AJ*, **142**, 102
- Graczyk D., et al., 2011, *Acta Astron.*, **61**, 103
- Green G. M., Schlafly E., Zucker C., Speagle J. S., Finkbeiner D., 2019, *ApJ*, **887**, 93
- Han Z., Podsiadlowski P., Maxted P. F. L., Marsh T. R., Ivanova N., 2002, *MNRAS*, **336**, 449
- Heinze A. N., et al., 2018, *AJ*, **156**, 241
- Henry G. W., Fekel F. C., Henry S. M., 2011, *AJ*, **142**, 39
- Huang C. X., et al., 2020a, *Research Notes of the American Astronomical Society*, **4**, 204
- Huang C. X., et al., 2020b, *Research Notes of the American Astronomical Society*, **4**, 206
- Jansen F., et al., 2001, *A&A*, **365**, L1
- Jayasinghe T., et al., 2019a, *MNRAS*, **486**, 1907
- Jayasinghe T., Stanek K. Z., Kochanek C. S., Thompson T. A., Shappee B. J., Fausnaugh M., 2019b, *MNRAS*, **489**, 4705
- Jayasinghe T., et al., 2021, *MNRAS*, **503**, 200
- Johnston C., Pavlovski K., Tkachenko A., 2019, *A&A*, **628**, A25
- Kahraman Aliçavuş F., Soyduğan E., Smalley B., Kubát J., 2017, *MNRAS*, **470**, 915
- Kaye A. B., Handler G., Krisciunas K., Poretti E., Zerbi F. M., 1999, *PASP*, **111**, 840
- Khangale Z. N., Woudt P. A., Potter S. B., Warner B., Kilkenny D., van der Heyden K., 2020, *MNRAS*, **495**, 637
- Kochanek C. S., et al., 2017, *PASP*, **129**, 104502
- Kostov V. B., et al., 2022, *ApJS*, **259**, 66
- Kovács G., Zucker S., Mazeh T., 2002, *A&A*, **391**, 369
- Kunimoto M., et al., 2021, *Research Notes of the American Astronomical Society*, **5**, 234
- Leiner E., Mathieu R. D., Geller A. M., 2017, *ApJ*, **840**, 67
- Li G., Van Reeth T., Bedding T. R., Murphy S. J., Antoci V., Ouazzani R.-M., Barbara N. H., 2020, *MNRAS*, **491**, 3586
- Lomb N. R., 1976, *Ap&SS*, **39**, 447
- Lurie J. C., et al., 2017, *AJ*, **154**, 250
- Marsh T. R., Armstrong D. J., Carter P. J., 2014, *MNRAS*, **445**, 309
- Marshall D. J., Robin A. C., Reylé C., Schultheis M., Picaud S., 2006, *A&A*, **453**, 635
- Mathieu R. D., van den Berg M., Torres G., Latham D., Verbunt F., Stassun K., 2003, *AJ*, **125**, 246
- Matijević G., Prša A., Orosz J. A., Welsh W. F., Bloemen S., Barclay T., 2012, *AJ*, **143**, 123
- Mazeh T., Shaham J., 1979, *A&A*, **77**, 145
- Østensen R. H., et al., 2010, *MNRAS*, **408**, L51
- Page M. J., et al., 2012, *MNRAS*, **426**, 903
- Pawlak M., et al., 2013, *Acta Astron.*, **63**, 323
- Pawlak M., et al., 2016, *Acta Astron.*, **66**, 421
- Pejcha O., Antognini J. M., Shappee B. J., Thompson T. A., 2013, *MNRAS*, **435**, 943
- Pejcha O., Cagaš P., Landri C., Fausnaugh M. M., De Rosa G., Prieto J. L., Henzl Z., Pešta M., 2022, arXiv e-prints, p. arXiv:2206.12456
- Petrosky E., Hwang H.-C., Zakamska N. L., Chandra V., Hill M. J., 2021, *MNRAS*, **503**, 3975
- Pojmanski G., 2002, *Acta Astron.*, **52**, 397
- Polsdofer E., Seale J., Sewilo M., Vjih U. P., Meixner M., Marengo M., Terrazas M., 2015, *AJ*, **149**, 78
- Pourbaix D., et al., 2004, *A&A*, **424**, 727
- Preece H. P., Hamers A. S., Battich T., Rajamuthukumar A. S., 2022, arXiv e-prints, p. arXiv:2209.11327
- Prša A., Zwitter T., 2005, *ApJ*, **628**, 426
- Prša A., et al., 2011, *AJ*, **141**, 83
- Prša A., et al., 2016, *ApJS*, **227**, 29
- Prša A., et al., 2022, *ApJS*, **258**, 16
- Rappaport S. A., et al., 2022, *MNRAS*, **513**, 4341
- Reed M. D., Foster H., Telting J. H., Østensen R. H., Farris L. H., Oreiro R., Baran A. S., 2014, *MNRAS*, **440**, 3809
- Reinhold T., Reiners A., Basri G., 2013, *A&A*, **560**, A4
- Ricker G. R., et al., 2015, *Journal of Astronomical Telescopes, Instruments, and Systems*, **1**, 014003
- Ritter H., Kolb U., 2003, *A&A*, **404**, 301
- Roettenbacher R. M., Kane S. R., Monnier J. D., Harmon R. O., 2016, *ApJ*, **832**, 207
- Rowan D. M., Stanek K. Z., Jayasinghe T., Kochanek C. S., Thompson T. A., Shappee B. J., Holoiën T. W. S., Prieto J. L., 2021, *MNRAS*, **507**, 104
- Rowan D. M., et al., 2022, arXiv e-prints, p. arXiv:2205.05687
- Scargle J. D., 1982, *ApJ*, **263**, 835
- Schmid V. S., Aerts C., 2016, *A&A*, **592**, A116
- Sepulveda A. G., Huber D., Zhang Z., Li G., Liu M. C., Bedding T. R., 2022, arXiv e-prints, p. arXiv:2205.01103
- Shappee B. J., et al., 2014, *ApJ*, **788**, 48
- Shi X.-d., Qian S.-b., Li L.-J., 2022, *ApJS*, **259**, 50
- Soszyński I., et al., 2010, *Acta Astron.*, **60**, 17
- Soszyński I., et al., 2011, *Acta Astron.*, **61**, 217
- Soszyński I., et al., 2015, *Acta Astron.*, **65**, 297
- Southworth J., Bowman D. M., 2022, *MNRAS*, **513**, 3191
- Southworth J., Van Reeth T., 2022, *MNRAS*, **515**, 2755
- Soyduğan E., İbanoğlu C., Soyduğan F., Akan M. C., Demircan O., 2006a, *MNRAS*, **366**, 1289
- Soyduğan E., Soyduğan F., Demircan O., İbanoğlu C., 2006b, *MNRAS*, **370**, 2013
- Stobie R. S., et al., 1997, *MNRAS*, **287**, 848
- Thompson S. E., et al., 2012, *ApJ*, **753**, 86
- Tkachenko A., et al., 2020, *A&A*, **637**, A60
- Tonry J. L., et al., 2018, *ApJ*, **867**, 105
- Torres G., Andersen J., Giménez A., 2010, *A&ARv*, **18**, 67
- Torres G., Sandberg Lacy C. H., Fekel F. C., Wolf M., Muterspaugh M. W., 2017, *ApJ*, **846**, 115
- Traulsen I., et al., 2020, *A&A*, **641**, A137
- Tremaine S., 2020, *MNRAS*, **493**, 5583
- Udalski A., Szymanski M., Kaluzny J., Kubiak M., Mateo M., 1992, *Acta Astron.*, **42**, 253
- Van Reeth T., Tkachenko A., Aerts C., 2016, *A&A*, **593**, A120
- Voges W., et al., 1999, *A&A*, **349**, 389
- Warner B., Woudt P. A., Pretorius M. L., 2003, *MNRAS*, **344**, 1193

- Webb N. A., et al., 2020, *A&A*, 641, A136  
Wrona M., et al., 2022, *ApJS*, 259, 16  
Yershov V. N., 2014, *Ap&SS*, 354, 97  
Zasche P., et al., 2019, *A&A*, 630, A128  
Zasche P., Henzl Z., Mašek M., 2021, *A&A*, 652, A81  
Zasche P., Henzl Z., Masek M., 2022, arXiv e-prints, p. [arXiv:2205.03934](https://arxiv.org/abs/2205.03934)  
Zhang B., et al., 2022, *ApJS*, 258, 26

## APPENDIX A: LIGHT CURVES OF SELECTED TARGETS

All light curves from Table 1 are available at <https://asas-sn.osu.edu/binaries>. Here we show example light curves to highlight different types of variability. Figure A1 shows additional examples of rotational variability where the spot behavior changes throughout and between TESS sectors. Figure A2 shows three examples of binaries with stochastic variability. Finally, Figure A3 shows additional examples on a Gaia CMD.

This paper has been typeset from a  $\text{\TeX}/\text{\LaTeX}$  file prepared by the author.



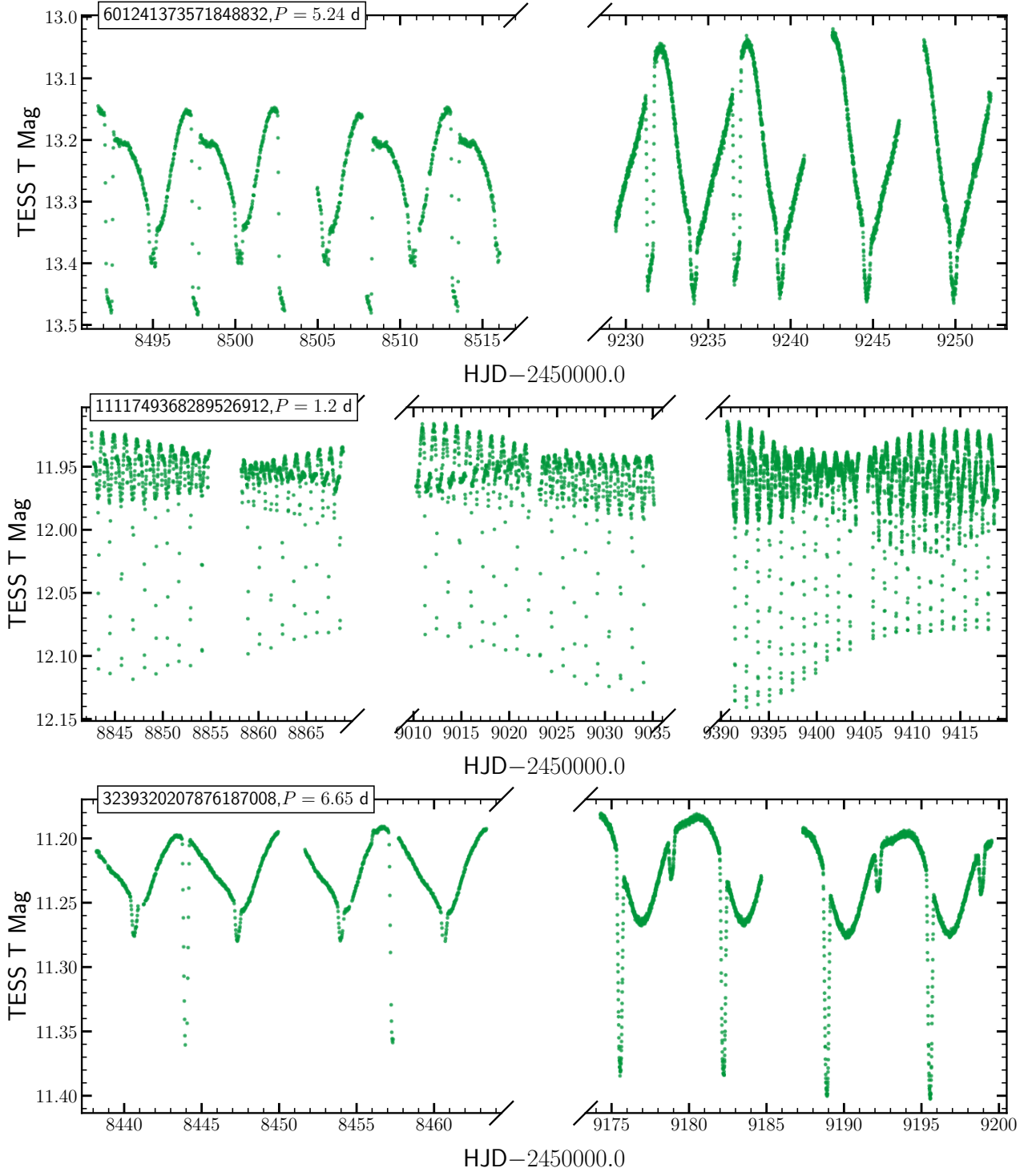


**Figure A1.** Three examples of spotted eclipsing binaries where there is clear rotational modulation in the TESS light curves. The orbital period and Gaia DR3 Source ID are given in the upper left of each panel.

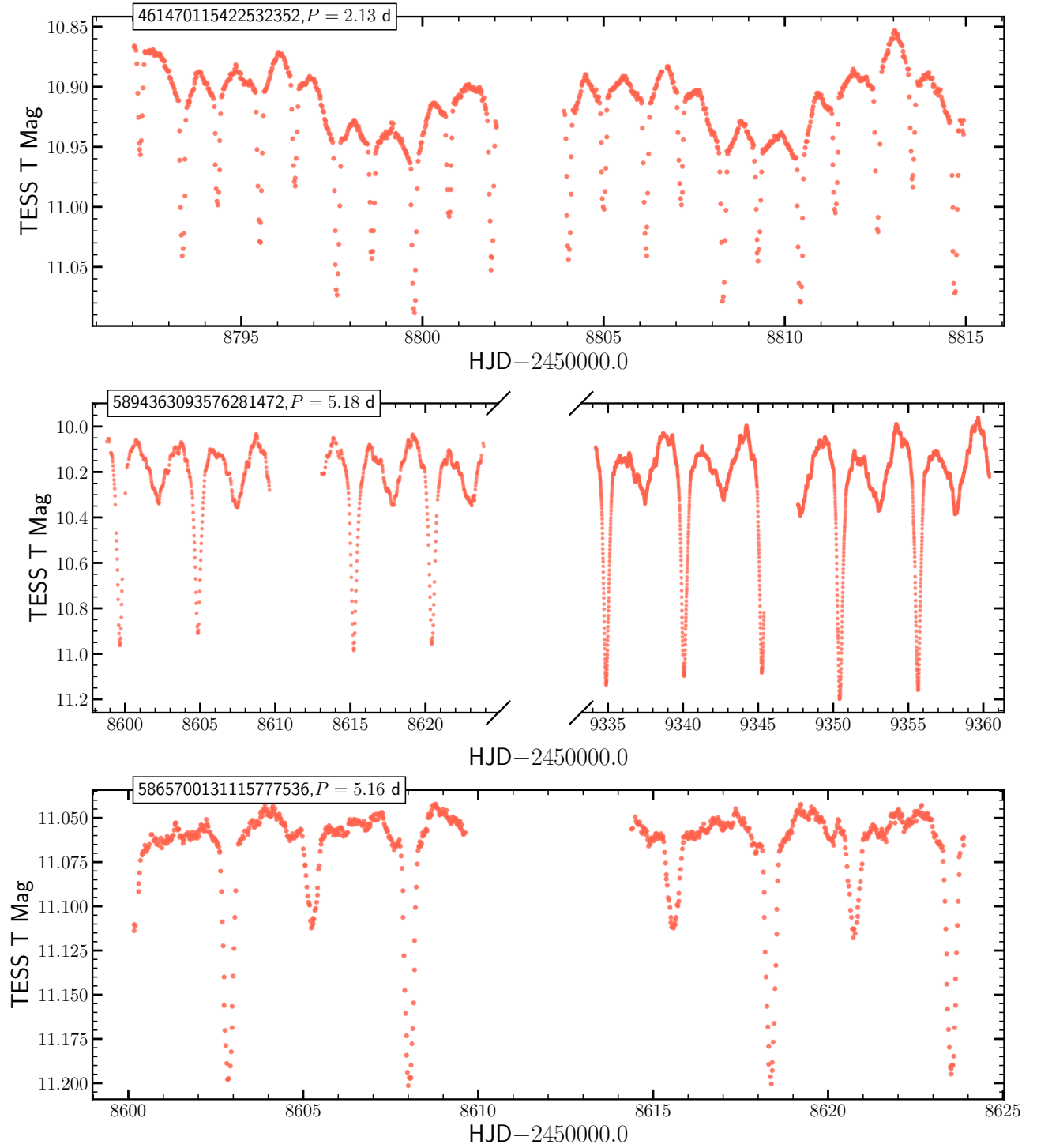


**Figure A2.** Three examples of TESS light curves for stochastically varying eclipsing binaries. The orbital period and Gaia DR3 Source ID are given in the upper left of each panel.

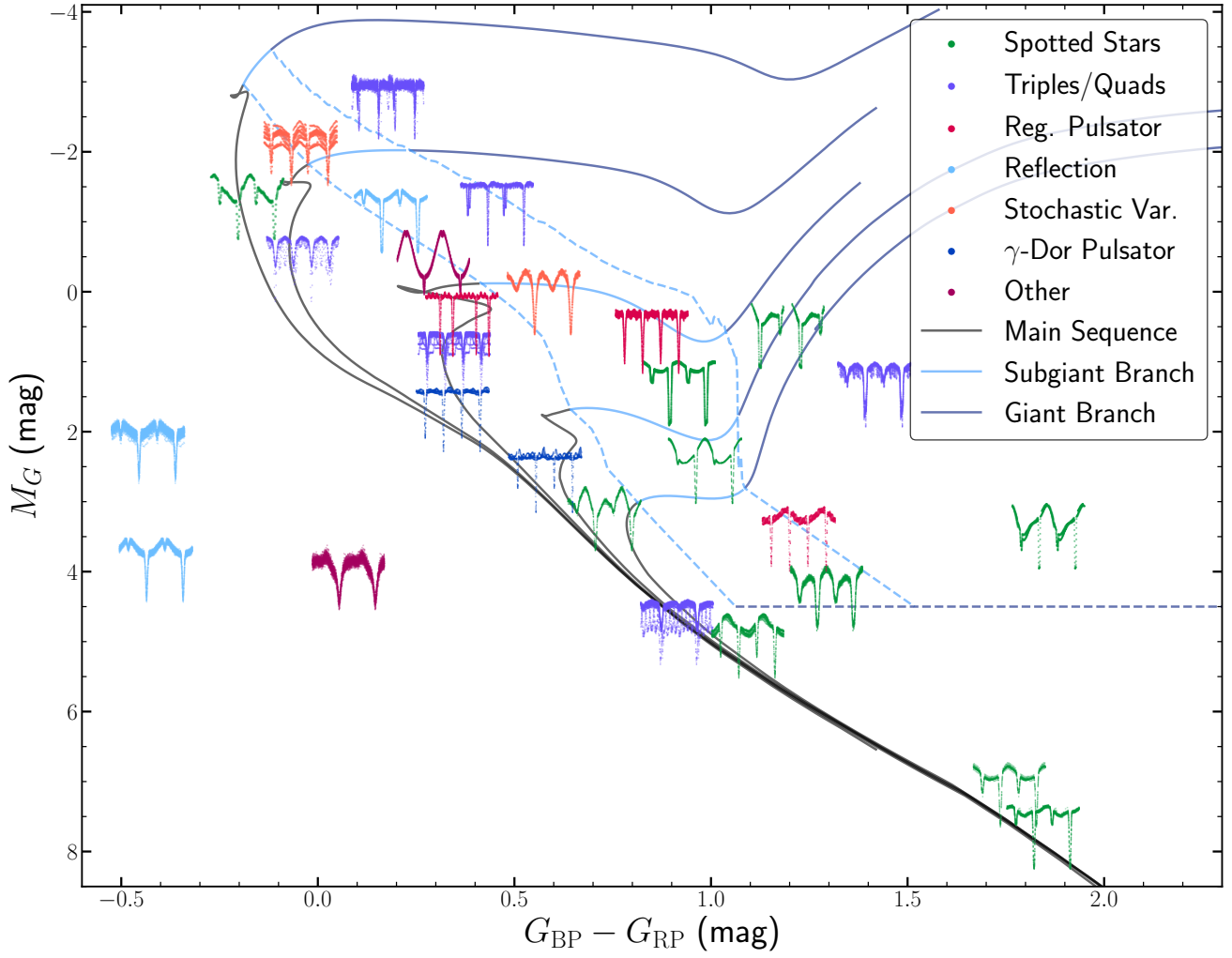


**Figure A3.** Examples of eclipsing binaries of different extra-physics types on a Gaia CMD.